Impacts of tectonic subsidence on basin depth and delta lobe building

Tian Yang Dong[1], Jeffrey Albert Nittrouer[2], Brandee Carlson[3], Brandon McElroy[4], Elena Il'icheva[5], Maksim Valirievich Pavlov[5], and Hongbo Ma[6]

[1]University of Texas at Austin
[2]Texas Tech University
[3]University of Houston
[4]University of Wyoming
[5]Laboratory of Hydrology and Climatology, V.B. Sochava Institute of Geography, Siberian Branch Russian Academy of Science (SB RAS)
[6]Tsinghua University

November 22, 2022

Abstract

Channel avulsions on river deltas are the primary means to distribute sediment and build land at the coastline. Many studies have detailed how avulsions generate delta lobes, whereby multiple lobes amalgamate to form a fan-shaped deposit. Physical experiments demonstrated that a condition of sediment transport equilibrium can develop on the topset, characterized by neither deposition nor erosion of sediment, and material is dispersed to the foreset. This alluvial grade condition assumes steady subsidence and uniform basin depth. In nature, however, alluvial grade is disrupted by variable subsidence, and progradation of lobes into basins with variable depth: conditions that are prevalent for tectonically active margins. We explore sediment dispersal and deposition patterns across scales using measurements of delta and basin morphology compiled from field surveys and remote sensing, collected over 150 years, from the Selenga Delta (Baikal Rift Zone), Russia. Tectonic subsidence events, associated with earthquakes on normal faults crossing the delta, displace portions of the topset several meters below mean lake level. This allogenic process increases regional river gradient and triggers lobe-switching avulsions. The timescale for these episodes is shorter than the predicted autogenic lobe avulsion timescale. During quiescent periods between subsidence events, channel-scale avulsions occur relatively frequently because of in-channel sediment aggradation, dispersing sediment to regional lows of the delta. The hierarchical avulsion processes, arise for the Selenga Delta, preserves discrete stratal packages that contain predominately deep channels. Exploring the interplay between discrete subsidence and sediment accumulation patterns will improve interpretations of stratigraphy from active margins and basin models.

Impacts of tectonic subsidence on basin depth and delta lobe building

Tian Y. Dong[1], Jeffrey A. Nittrouer[2], Brandee Carlson[3], Brandon McElroy[4], Elena Il'icheva[5], Maksim Pavlov[5], Hongbo Ma[6]

[1]Department of Geological Sciences, Jackson School of Geosciences, University of Texas at Austin, 23 San Jacinto Blvd., Austin, Texas 78712, U.S.A

[2]Department of Geosciences, Texas Tech University, Mail Stop 1053, Lubbock, Texas 79409, U.S.A

[3]Department of Earth and Atmospheric Sciences, University of Houston, 3507 Cullen Blvd., Houston, TX 77204, U.S.A.

[4]Department of Geology and Geophysics, University of Wyoming, 1000 E. University Ave., Laramie, Wyoming 82071, U.S.A

[5]Laboratory of Hydrology and Climatology, V.B. Sochava Institute of Geography, Siberian Branch Russian Academy of Sciences, 1 Ulan-Batorskaya Street, Irkutsk, 664033, Russian Federation

[6]Henry Samueli School of Engineering, University of California Irvine, Engineering Hall 5400, Irvine, California 92697, U.S.A

Key Points:

- Tectonic subsidence produces variable receiving basin depth, and drives lobe-scale avulsions by modifying delta-topset gradient
- Channel-scale avulsions occur during periods of tectonic quiescence, and disperse sediment to nourish the deltaic shoreline
- Hierarchical avulsion processes could lead to preservation of discrete stratal packages that contain predominately deep channels

Corresponding author: Tian Y. Dong, `tian.y.dong@utexas.edu`

Abstract

Channel avulsions on river deltas are the primary means to distribute sediment and build land at the coastline. Many studies have detailed how avulsions generate delta lobes, whereby multiple lobes amalgamate to form a fan-shaped deposit. Physical experiments demonstrated that a condition of sediment transport equilibrium can develop on the topset, characterized by neither deposition nor erosion of sediment, and material is dispersed to the foreset. This alluvial grade condition assumes steady subsidence and uniform basin depth. In nature, however, alluvial grade is disrupted by variable subsidence, and progradation of lobes into basins with variable depth: conditions that are prevalent for tectonically active margins. We explore sediment dispersal and deposition patterns across scales using measurements of delta and basin morphology compiled from field surveys and remote sensing, collected over 150 years, from the Selenga Delta (Baikal Rift Zone), Russia. Tectonic subsidence events, associated with earthquakes on normal faults crossing the delta, displace portions of the topset several meters below mean lake level. This allogenic process increases regional river gradient and triggers lobe-switching avulsions. The timescale for these episodes is shorter than the predicted autogenic lobe avulsion timescale. During quiescent periods between subsidence events, channel-scale avulsions occur relatively frequently because of in-channel sediment aggradation, dispersing sediment to regional lows of the delta. The hierarchical avulsion processes, arise for the Selenga Delta, preserves discrete stratal packages that could contain predominately deep channels. Exploring the interplay between discrete subsidence and sediment accumulation patterns will improve interpretations of stratigraphy from active margins and basin models.

Plain Language Summary

River deltas distribute sediment and build land in coastal regions via abrupt shifts in course through a process called channel avulsion. The fan-shaped morphology of river deltas arises from multiple avulsion events. Our understanding of how deltas build such morphology often assumes that size of the downstream reservoir, such as a lake or ocean, is constant over time. However, geological activity like earthquakes changes the reservoir size by displacing the reservoir bottom. We complied and analyzed 150 years of delta morphology data from the Selenga Delta in Russia to understand how changing reservoir size impacts channel avulsion process. We found that two distinct avulsion process

arise for the Selenga Delta: a regional scale avulsion that is impacted by earthquakes and a local scale avulsion that is caused by sediment deposition in the channel. The two scales of avulsions work together to shape the morphology of the delta system. In addition, avulsions produce unique subsurface records that can be used to understand the history of a delta. Our work highlights the importance of understanding the variability in downstream reservoir size to predict future change in delta morphology.

1 Introduction

River deltas prograde basinward by distributing sediment over the topset and foreset. A major contributor to spatiotemporal variability in dispersal are channel avulsions, which relocate channels and depocenters (Swenson, 2005; W. Kim et al., 2010; Reitz & Jerolmack, 2012; Chadwick et al., 2019). With multiple avulsions, delta lobes amalgamate to produce a semicircular fan shape that continues to be nourished by the distributary channel network (Ganti et al., 2014; Piliouras et al., 2017; Carlson et al., 2018; Moodie et al., 2019). Theoretical and experimental evidence suggests that, over time, delta lobe growth reaches a state of sediment transport equilibrium, known as alluvial grade, characterized by sediment bypass of the topset with delivery to the foreset (Richards et al., 1998; Posamentier & Allen, 1999; Y. Kim et al., 2013; Muto et al., 2016; Carlson et al., 2018). Alluvial grade and channel avulsions are impacted by autogenic and/or allogenic processes that alter upstream and downstream boundary conditions, thereby affecting delta steady-state dynamics (Wang et al., 2019). Constraining the interplay of these processes over a range of timescales is thus critical to improving delta evolution models. Such scientific developments are useful in various modern settings to combat land loss, as well as in ancient settings to evaluate stratigraphy (W. Kim et al., 2006; Syvitski et al., 2009; Straub et al., 2009; W. Kim et al., 2009).

Alluvial grade of a delta lobe can be assessed using the grade index (G_{index}; Muto et al., 2016):

$$
\begin{aligned}
G_{index} =& \frac{1}{1 + 2h_* + \alpha_* h_*^2}, \\
\alpha_* =& \frac{S_{fan}}{S_{basin}}, \\
h_* =& \frac{H_{basin}}{\bar{R} S_{fan}},
\end{aligned}
\tag{1}
$$

where α_* and h_* are normalized delta topset slope and basin water depth, respectively, S_{fan} is topset slope, S_{basin} is basin slope, H_{basin} is basin depth, and $\bar{R}$ is the mean delta radius. Herein, $G_{index} \rightarrow 0$ indicates a river delta achieved alluvial grade and $G_{index} \rightarrow 1$ indicates sediment imbalance. Since most delta systems have relatively low topset gradients and flow depth, basin depth (H_{basin}) is one of the most important parameters that impacts alluvial grade. This variable is often affected by tectonic subsidence (Carlson et al., 2018). For example, deltas on active margins usually maintain deep basin depth, and therefore achieve alluvial grade, whereby aggradation on the topset is negligible and distributary channels are immobile and possess well-developed levees (Muto et al., 2016; Wang et al., 2019). While accommodating sediment dispersal to the foreset, a deep receiving basin depth limits shoreline progradation because it takes longer to fill the space at the delta front (Carlson et al., 2018).

Alluvial grade also affects the development of stratigraphy. Specifically, stratigraphic completeness, i.e., the preservation of genetically related fluvial-deltaic facies from proximal topset to distal foreset, is viewed as a competition between accommodation and sediment supply (Straub et al., 2013). Deltas at alluvial grade may preferentially preserve strata in the foreset due to limited topset aggradation (Y. Kim et al., 2013). Stratigraphic completeness of delta deposits could be approximated by the filling index, B (Liang et al., 2016):

$$B = \frac{dV_{accomm.}/dt}{Q_{supply}}, \tag{2}$$

where $dV_{accomm.}/dt$ is the change volume of accommodation, per-unit-time, generated by subsidence, and is closely associated with basin depth (H_{basin}). Q_{supply} is sediment supply. When $B > 1$, accommodation outpaces sediment supply, and delta progradation is limited; conversely, when $B < 1$, sediment supply outpaces accommodation, facilitating delta progradation (W. Kim et al., 2010; Straub et al., 2013; Kopp & Kim, 2015; Reitz et al., 2015; Liang et al., 2016).

Alluvial grade also affects the size of preserved sedimentary structures, such as lateral accretions produced by mobile channels. For example, immobile distributary channels of deltas at alluvial grade and morphodynamic reworking of bedform deposits preferentially preserve the largest dunes developed deposited during flood events (Ganti et al., 2020; Wu et al., 2021). One way to quantify the preservation potential of different sedimentary structures is to use the preserved extremality index (Ω), a metric ranging from 0 to 1 (Ganti et al., 2020):

$$\Omega = \frac{100 - 2\tilde{p}}{100}, \tag{3}$$

where $\tilde{p}$ is the median percentile of the preserved topography (size of sedimentary structure). $\Omega \to 1$ indicates that large sedimentary structures deposited during low frequency, high magnitude events dominate preserved strata; conversely, $\Omega \to 0$ indicates that deposits formed during high frequency, low magnitude events, i.e., “ordinary features”, dominate preserved stratigraphy.

Two assumptions are often made about alluvial grade and development of deltaic stratigraphy: time-continuous subsidence and uniform receiving basin depth (e.g., Liang et al., 2016). In nature, however, basin geometry is modified by spatially variable subsidence and filling of accommodation. In tectonic settings, for example, multiple faults may be active, generating variable receiving basin depth (Martinsen & Bakken, 1990; C. Scholz et al., 1998; Shchetnikov et al., 2012; Vologina et al., 2010; Dong et al., 2016). Rift basins are well-documented sediment sinks, however, the impacts of tectonic subsidence and variable basin depth on delta lobe building remains elusive (Ravnås & Steel, 1998). Field evidence indicating how delta morphology and lobe growth are impacted by alluvial grade is also limited (Y. Kim et al., 2013; Ganti et al., 2014; Muto et al., 2016; Wang et al., 2019).

Herein, data from the Selenga River delta are used to assess the effects of tectonic subsidence on basin depth and delta lobe building over 150 years. Specifically, existing theory for alluvial grade is applied to better understand how tectonic subsidence modifies basin depth, delta topset morphology, shoreline position, sediment transport, and avulsion timescales. These findings are leveraged with literature-compiled subsurface evidence from the Selenga Delta to describe stratigraphic completeness and morphodynamic hierarchy about the Selenga system specifically, and deltas on active margins broadly.

2 Lake Baikal and the Selenga River delta

The Selenga River delta is located at the southeastern shore of Lake Baikal, Russia (Figure 1a; Colman, 1998; C. Scholz et al., 1998; Il’icheva et al., 2015). This basin is formed by rifting that initiated ∼35 million years ago (Logatchev, 1974; C. Scholz et

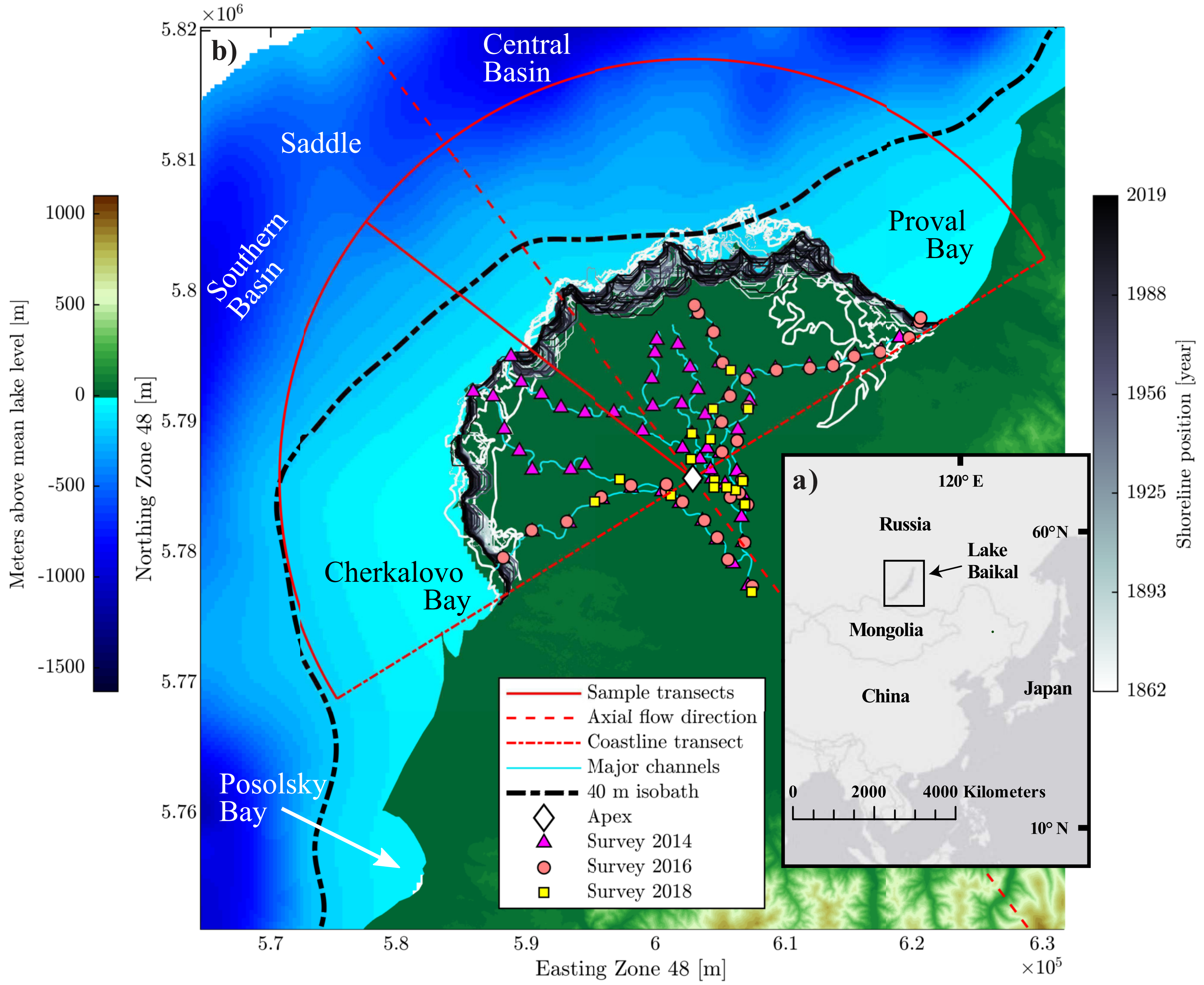

Figure 1. a) Lake Baikal and the Selenga River delta, located in southeastern Siberia, Russia. b) Bathymetric map of Lake Baikal and digital elevation model of the landscape produced from NASA SRTM data. Deltaic shorelines are extracted from images collected by Landsat missions (3, 5, 8) and historical surveys, spanning 157 years, from 1862 to 2019. A semicircular sampling grid, centered at the delta apex (white diamond), is used to measure attributes of the delta and basin morphology. A total of 180 radial sampling transects, spaced at 1° lobe opening angle (Θ) and originated from the delta apex, are used to make profiles in Figures 6 and 7 (solid read line as example). $\Theta = 0°$ at the westernmost transect and $\Theta = 180°$ at the easternmost transect. Hydrological data are collected from the seven main distributary channels shown on the map.

al., 1998; Logachev, 2003; Mats & Yefimova, 2015; Krivonogov & Safonova, 2017). Lake Baikal's water level has remained relatively stable and the mean lake volume is interpreted to be roughly constant for over the past ∼100 k.y. (Colman, 1998; C. Scholz et al., 1998). Additionally, there is no evidence for major tectonism that would substantially modify the basin configuration and potentially impact lake volume during the last 100 k.y. (Logachev, 2003; Krivonogov & Safonova, 2017). Seismic imaging indicates that sediment thickness is 4–5 km in the South Baikal Basin, and 7.5–10 km in the modern Selenga Delta front (Hutchinson et al., 1992). The variable thickness of sediment accumulation, and underlying bedrock highs and lows, have created a bathymetric saddle between the South Baikal Basin and Central Baikal Basin, where the Selenga Delta is situated (Figure 1b; Hutchinson et al., 1992; C. A. Scholz & Hutchinson, 2000).

The delta channel network maintains variable bed and bank sediment size, vegetation, and morphology across the alluvial topset, extending 35 km from the apex, to the delta shoreline (Il'icheva, 2008; Il'icheva et al., 2015; Dong et al., 2016; Pietroń et al., 2018; Dong et al., 2019, 2020). Both median bed- and bank-sediment grain size fine downstream, from gravel at the apex to silt and very-fine sand at the shoreline (Dong et al., 2016).

On timescales of $10^2 - 10^3$ years, delta morphology is influenced by seismic events. Specifically, a portion of the subaerial delta subsides by up to 4 m (Shchetnikov et al., 2012; Lunina & Denisenko, 2020), a length that exceeds the mean distributary channel depth (2.7 m) of the delta (Dong et al., 2019). For example, in association with recent (1862) seismic event (M 7.5), 200 km^2 of the delta downdropped by ∼3 m, forming Proval Bay (Figure 1b; Vologina et al., 2007, 2010; Lunina & Denisenko, 2020). This subsidence event steepened the regional slope and drove a lobe avulsion that diverted water and sediment from central region of the delta to fill the newly formed bay (Figure 1b).

Several additional embayments have been formed similarly, and are distributed around the delta, including Cherkalovo and Posolsky Bays (Figure 1b; Shchetnikov et al., 2012). Cherkalovo Bay has an age range between 1765±235 and 2905±205 years before present, based on ΔC_{14} dates from sediment cores (Pavlov et al., 2019). Posolsky Bay, just south of the delta, formed ∼500−600 years ago (Figure 1b; Shchetnikov et al., 2012). Based on these historical records, the recurrence interval of morphologically impactful earthquakes that creates embayments on the delta is 340−2600 years (Table 1). We refer to this interval as the tectonic timescale (T_t) in discussions below.

3 Methods

3.1 Remote sensing analysis

Basin and delta-lobe characteristics of the Selenga River delta, including shoreline position and avulsion locations, were measured using remote sensing methods, to evaluate alluvial grade and estimate avulsion timescales. Bathymetry of Lake Baikal and embayments adjacent to the Selenga Delta (Proval and Cherkalovo Bays) were used to measure basin depth and slope (Figure 1; DeBatist & Charlet, 2007; Vologina et al., 2007, 2010; Pavlov et al., 2019). Digital Elevation Models (DEM), created by NASA Shuttle Radar Topography Mission (SRTM), were used to measure topset slope. Manually georeferenced historical survey maps ($n = 4$, collected in 1862, 1908, 1956, and 1962; Galazy, 1993; Il'icheva, 2008; Vologina et al., 2007, 2010; Shchetnikov et al., 2012; Il'icheva et al., 2015) and 141 cloud-free Landsat (3, 5, 8) sensor measurements from 1975 to 2019, were used to constrain changes in shoreline and locations of channel avulsion.

A DEM combining bathymetric and topographic data was created and used to generate elevation profiles that were measured radially based on a semicircular sampling grid with a 180° opening angle, extending from the delta apex to the lake bottom (Figure 1). Datum of the bathymetric and topograhic data were relative to the Baltic sea level and mean global sea level, respectively, and were projected to UTM zone 48N (DeBatist & Charlet, 2007). By setting a 1° grid spacing, a total of 180 radial sampling transects were established (Figure 1). The grid center was set at the delta apex, defined as the intersection between the axial flow direction of the Selenga River and the adjacent Lake Baikal shoreline (Figure 1).

3.1.1 Measuring basin and delta characteristics: slope and depth

Basin slope (S_{basin}) was measured between the delta shoreline and location of maximum curvature of the bathymetric profile (Figure 2). Basin depth (H_{basin}) was defined as the water depth at the location of maximum curvature. For earthquake-impacted (subsided) regions of the delta, basin depth was defined as water depth of the adjacent embayments (Figure 2). To measure solely land elevations, channel pixels (mapped during moderate water discharge, $Q_w = 1100$ m^3/s) are excluded from SRTM data. Topset slope (S_{fan}) was measured from the delta apex to the shoreline along sampling transects.

3.1.2 Quantifying shoreline change

Historical maps and satellite images were used to document the shoreline position of the delta. Shorelines were traced manually from georeferenced historical maps in ArcGIS. For Landsat images, land and water were differentiated using a modified Normalized Difference Water Index (MNDWI), by combining shortwave near-infrared and green bands (Xu, 2006). Shorelines were then extracted automatically from the MNDWI images and manually checked for quality (Moodie et al., 2019). Delta radius was measured as the distance between shoreline and apex for the 180 transects per Landsat image. Annual mean delta radius ($\bar{R}$) was used to calculate long-term mean progradation rates ($\bar{R}_{pro}$) over the period of 1862−2019 via a linear relationship between time and shoreline positions (Moodie et al., 2019). Similarly, decadally averaged position were calculated ($\bar{R}_{pro,d}$). Note that data availability is sparse during the period of 1862−1986 (i.e., prior to Landsat 5 mission). As a result, two measurements of mean radius during this period were spaced by 90 and 20 years, respectively. For the period of 1986−2019 (Landsat Missions 5 and 8), measurements of decadal mean raidus were spaced by 10 years. Finally, total change in delta radius ($\Delta\bar{R}$) was calculated by differencing shoreline positions for 1862 and 2019.

3.1.3 Identifying avulsion sites

To identify avulsion locations, 141 MNDWI images were stacked to generate a water occupation frequency map, an index defined as the fraction of time that a given spatial location (image pixel) is occupied by water (W. Kim et al., 2006; Straub et al., 2013; Piliouras et al., 2017; Aminjafari et al., 2021). This index was then normalized by its maximum value, yielding a normalized water occupation frequency map (NWOF). In particular, new flow pathways had low NWOF values. The NWOF map and Landsat images were examined visually to identify avulsion sites, defined as the formation of a new channel pathway (D. A. Edmonds et al., 2011).

3.2 Field measurements

Width, and depth were measured in seven major distributary channels of the Selenga Delta, using a LOWRANCE single-beam sonar to collect cross-sections over low to bankfull flow conditions during three field expeditions from 2014 to 2018 (60 transects total; Figure 1; Dong et al., 2016, 2019, 2020). At each location, water surface, channel bank and bed elevation were measured using a JAVAD differential Global Navigation Satellite System. These transects were spaced 2.5−4 km (Figure 1). In 2018, water and sediment discharge at 16 sites, located same as the previous surveys, were monitored for 2.5 months to measure flow partitioning in the delta distributary network (Q_w = 900−2300 m^3/s; Figure 1; Dong et al., 2020).

3.3 Distinguishing delta lobes

A graph theory approach is used to identify delta lobes (Dong et al., 2020). Steady-state flux of the Selenga Delta channel network is approximated using a rooted directed acyclic graph (G), such that $G = (V, E)$ (Tejedor et al., 2015a, 2015b; Dong et al., 2020). V and E are a collection of vertices and links, respectively. Channels are defined as links. Bifurcation and confluence nodes, and channel outlets at the shoreline, are represented by vertices. Link directions correspond to channel flow direction, from the delta apex to the shoreline. Each link contains hydraulic information, such as channel width, and is used to predict flow partitioning (F) for the entire network. A contributing subnetwork is identified for each channel outlet, which contains all the links and vertices that contribute flux to it. Subnetworks can be grouped together as a delta lobe based on the proportion of shared flux using dynamic pairwise dependence (DPD; Tejedor et al., 2015b):

$$DPD_{ij} = \frac{\sum_{u \in S_{ij}} F(u)}{\sum_{v \in S_i} F(v)}; \tag{4}$$

here, S_i is the set of links that belong to subnetwork i with vertices of u. S_{ij} is the set of links that belong to both subnetwork i and j, with vertices of v. High DPD values indicate that two subnetworks share a large amount of flux. Using this metric, channel outlets and their associated upstream links and vertices are grouped together based on the proportion of shared flux.

3.4 Constraining lobe volumes

A geometrical framework is used to evaluate change in sediment volume of the delta lobes, following Muto et al. (2016). Assuming sediment balance (V_t):

$$(1 - \lambda_p) \int_0^t Q_s dt = V_{ae} + V_{aq} = V_t. \tag{5}$$

Q_s is the long-term mean sediment discharge in unit of m^3/yr, V_{ae} and V_{aq} are the subaerial and subaqueous sediment volumes, respectively. λ_p is the porosity of unconsolidated mixed sand and gravel, $\lambda_p = 0.25$ (Leopold et al., 1964; Dong et al., 2016). Assuming a horizontal basement and a constant sediment discharge, V_{ae} is calculated as a half-cone (Figure 2; Reitz & Jerolmack, 2012; Muto et al., 2016):

$$V_{ae} = \frac{\lambda}{6} h \bar{R}^2, \tag{6}$$

where λ is the delta lobe spreading angle in radians, h is sediment thickness at the delta apex above a datum, and is set as the mean lake level (455 m), $h = \bar{S}_{fan}\bar{R}$, where $\bar{R}$ is the mean delta lobe radius and $\bar{S}_{fan}$ is the mean topset slope. V_{aq} is constrained by a truncated half-cone (Figure 2; Wang et al., 2019):

$$V_{aq} = \frac{\lambda}{2} \bar{H}_{bay} \bar{R}^2 + \frac{\lambda}{2S_{fore}} \bar{H}_{bay}^2 \bar{R} + \frac{\lambda}{6S_{fore}^2} \bar{H}_{bay}^3, \tag{7}$$

where $\bar{H}_{bay}$ is the mean water depth in the embayments, and S_{fore} is the foreset slope. For areas impacted by tectonic subsidence, basin slope is equivalent to foreset slope, and assumed to be at angle of repose for fine-grained sediment at 30°−32° (Piliouras et al., 2017; Wang et al., 2019).

Calculating the subaerial sediment volume before the 1862 earthquake (i.e., initial time, t_0) requires information about topset slope (S_{fan,t_0}) and sediment thickness (h_{t_0}) at the delta apex, which are difficult values to constrain at t_0. Assuming delta progradation over time, two scenarios bounding possible initial thicknesses and slopes are considered (Figure 2): $h > h_{t_0}$, so that the delta maintains a constant topset slope, $h_{t_0} = S_{fan}\bar{R}(t_0)$; and $S_{fan} < S_{fan,t_0}$, whereby sediment thickness at the apex is constant in time, $\bar{S}_{fan,t_0} = h/\bar{R}(t_0)$. Sediment fill since the earthquake is calculated for both scenarios as $\Delta V_t = V_{t,2019} - V_{t,1862}$.

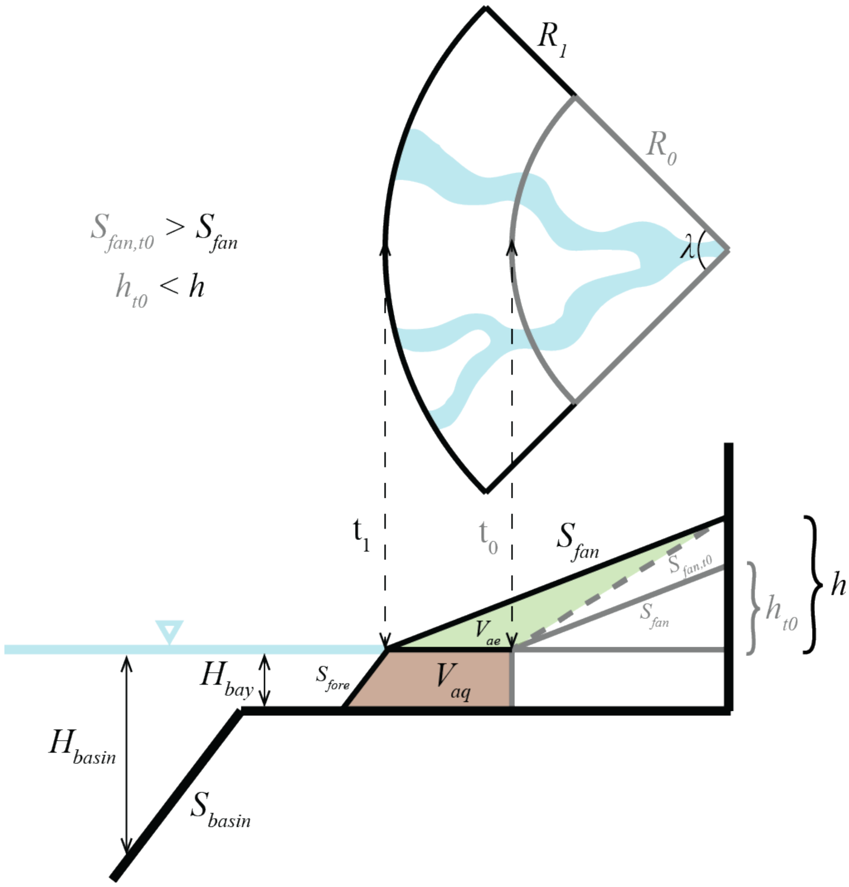

Figure 2. Sketch of an idealized delta used to calculate lobe volume (after Muto et al., 2016). A range of topset slopes (S_{fore}) and sediment thicknesses (h) at the delta apex were used to calculate sediment volume since 1862 (see main text). Note that the topset slope in 1862 ($S_{fan,t0}$) is greater than the topset slope at present (S_{fan}), with respective sediment thicknesses.

3.5 Sediment discharge

Total sediment load ($Q_{t,pred.}$) entering the delta is constrained by combing a sediment rating curve and historical hydrograph data, both of which were measured at the main stem from 1938 to 2015 (Figures 3a and c; S. R. Chalov et al., 2015; Pietroń et al., 2018; Dong et al., 2020). The long-term mean annual sediment discharge (Q_s) is calculated:

$$Q_s = \frac{1}{t}\int_0^t Q_{t,pred.} dt, \tag{8}$$

where $t = 78$ years is the duration of the historical hydrograph data. Bed material load (Q_{bm}) is calculated by removing the mud fraction (grain size < 0.0625 mm; 78.7%) from Q_s, based on the grain size distributions of suspended material measured at the main stem (Figure 3b; Nittrouer & Viparelli, 2014; S. Chalov et al., 2016). Since channel avulsions are driven by bed material aggradation, Q_{bm} is used to approximate in-channel aggradation rates and to estimate avulsion timescales (Mohrig et al., 2000).

3.6 Constraining both lobe and channel avulsion timescales

To consider the impacts of variable basin depth on delta building processes, the avulsion timescales of the delta lobes ($T_{A,l}$) were calculated as (Muto et al., 2016; Wang et al., 2019):

$$\begin{aligned} T_{A,l} &= \frac{T_{A,l,H_{basin}\sim 0}}{G_{index}}, \\ T_{A,l,H_{basin}\sim 0} &= \frac{\lambda \beta H_{bf,apex} \bar{R}^2}{2FQ_{bm}} \end{aligned} \tag{9}$$

where $T_{A,l,H_{basin}\sim 0}$ is the lobe avulsion timescale at zero basin depth, $H_{bf,apex}$ is bankfull depth at the delta apex, F is the fraction of sediment discharge that each lobe receives and is constrained using historical and field data (Table 1; Il'icheva, 2008; S. Chalov et al., 2016; Dong et al., 2020), and β is a coefficient that describes the fraction of in-channel aggradation required to setup an avulsion relative to the mean flow depth, and varies between 0.3 and 1 (Mohrig et al., 2000; Jerolmack & Mohrig, 2007; Ganti et al., 2014, 2016; Moran et al., 2017; Moodie et al., 2019; Chadwick et al., 2019). β is unconstrained, so T_A is calculated for a range of values, from $0.3-1$.

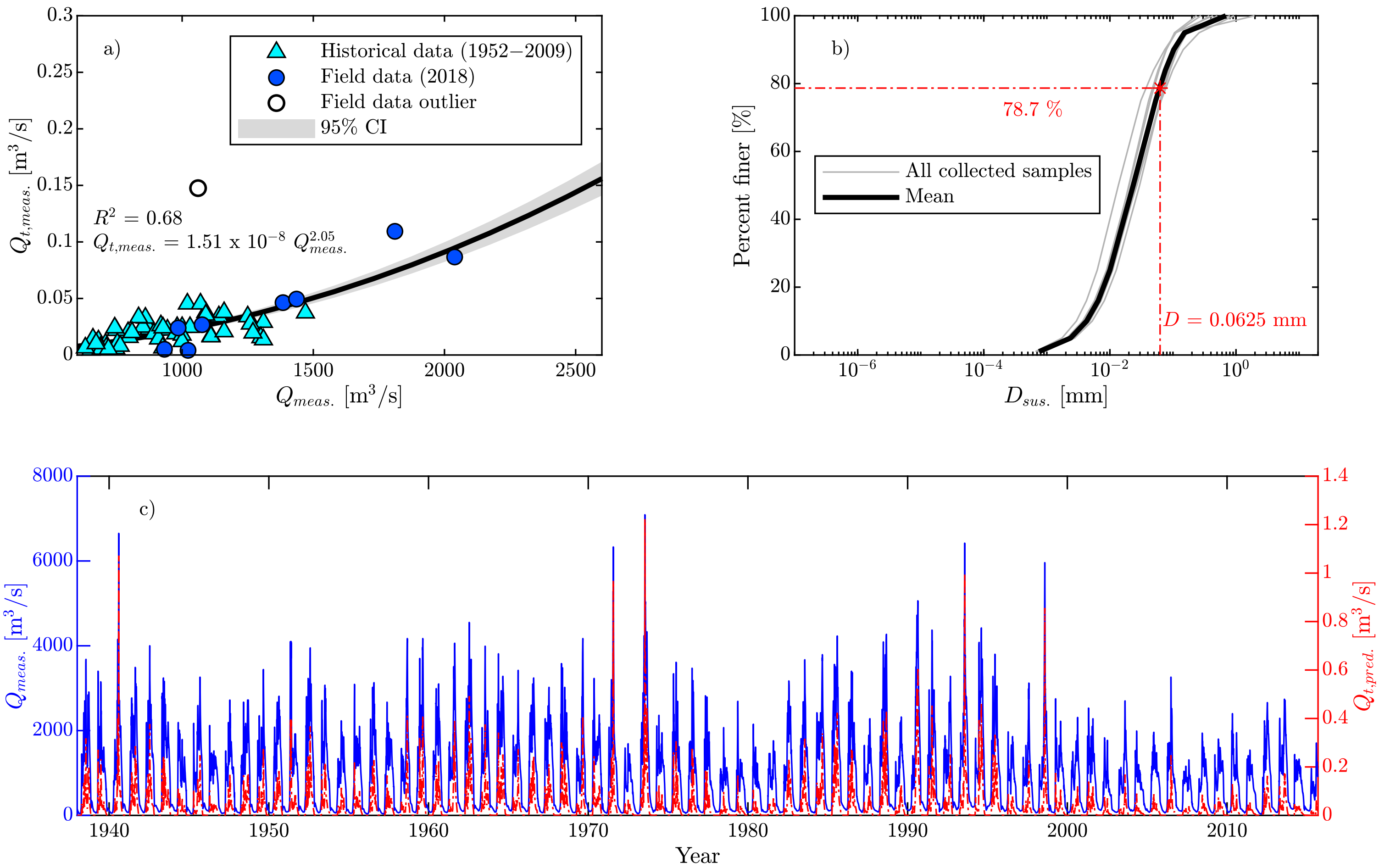

Figure 3. a) Rating curve of total sediment load ($Q_{t,meas.}$) measured for the Selenga Delta main stem (S. R. Chalov et al., 2015; Dong et al., 2020). b) Grain size distributions of suspended sediment at the main stem (S. Chalov et al., 2016). c) Water discharge ($Q_{meas.}$) and predicted total sediment load ($Q_{t,pred.}$) of the Selenga Delta main stem from 1938−2015 (Pietroń et al., 2018).

Interestingly, terraces exist near the delta apex (Gyninova & Korsunov, 2006; Dong et al., 2019). Stage and elevation surveys by Dong et al. (2019) revealed that the modern bankfull stage is 0.33±0.19 m below the bank terrace surfaces, consistent with Gyninova and Korsunov (2006), who also documented terraces that are 0.5−2.5 m higher than flood stage. Therefore H_{bf} is modified by terrace height to account for the distance between channel bed and terrace surface (Equation 9).

For smaller-scale distributary channels downstream of the terraces, the characteristic channel avulsion timescale ($T_{A,c}$) is calculated as (Reitz et al., 2010):

$$T_{A,c} = \frac{\beta \bar{L}_c \bar{B}_{bf} \bar{H}_{bf}}{Q_{bm,c}}, \tag{10}$$

where $\bar{L}_c$, $\bar{B}_{bf}$, and $\bar{H}_{bf}$ are mean channel length, bankfull width and depth measured from distributary channels within each delta lobe, respectively. $\bar{Q}_{bm,c}$ is the mean bed material load per channel:

$$\bar{Q}_{bm,c} = \frac{Q_{bm} F}{N}, \tag{11}$$

where N is the number of outlets for each lobe and F is the fraction of water and sediment discharge that each lobe partitions relative to the main river (S. Chalov et al., 2016; Dong et al., 2020).

A Monte Carlo approach was used to account for stochasticities in delta lobe and basin variables, such as shoreline position, as well as uncertainties in data collection and calculation. Specifically, probability distributions of delta lobe and basin variables were generated (i.e., parameters in Equations 1 and 5−11), measured from the 180 survey transects (Figure 1). These variables were randomly sampled 1 x 10^6 times to generate probability distributions of sediment volume (ΔV_t), grade index (G_{index}), lobe and channel avulsion timescales ($T_{A,l}$ and $T_{A,c}$, respectively) for each delta lobe via Equations 1 and 5−11. The full distribution, as well as the median and 25th and 75th percentiles (quartiles one and three) are reported in discussions below.

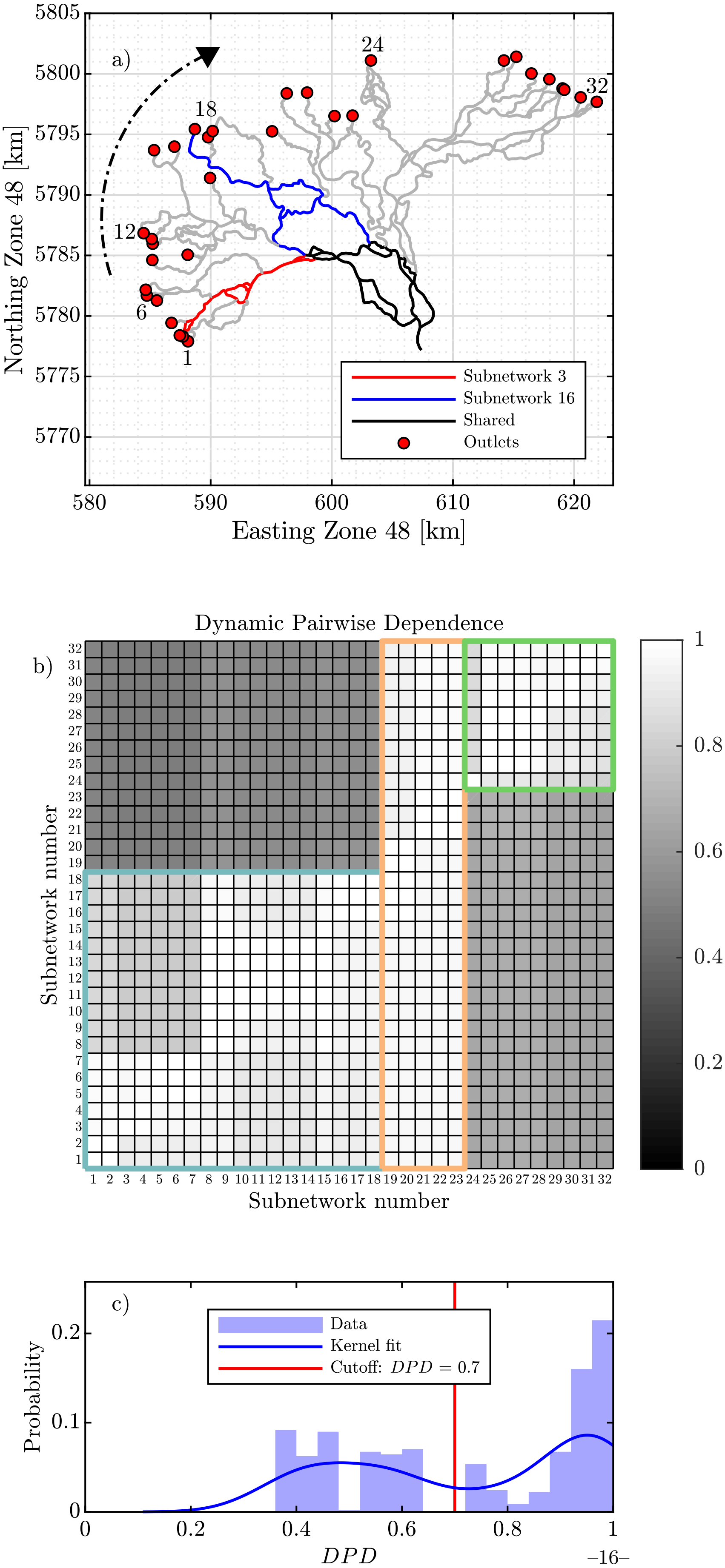

Figure 4. a) Examples of subnetworks on the Selenga Delta, differentiated using a graph theory framework (Tejedor et al., 2015a). b) Dynamic pairwise dependence (DPD) matrix used to distinguish lobes within the delta network. Rows and columns are set by the number of delta outelts (subnetworks). DPD values represent the proportion of flux shared between two subnetworks. Regions of symmetry along the diagonal represent a high proportion of shared flux. Interpreted delta lobes are highlighted by boxes with thick outlines. Color scheme of the lobes are consistent for subsequent figures. c) Probability distribution of DPD values. Two populations emerged, separated by a cutoff value, $DPD = 0.7$.

4 Results

4.1 Identification of delta lobes

A total of 32 vertices are identified as outlets using the graph theory framework, as they are connected to Lake Baikal or to a surrounding embayment (Figure 4a). Outlets are indexed consecutively and clockwise, starting with the westernmost location (Figure 4a). A subnetwork is identified for each outlet and is compared to its 31 neighbors based on the proportion of shared flux (Figure 4a), yielding a 32 x 32 dynamic pairwise dependence matrix (DPD). Two distinct populations emerge from the probability distribution of DPD, separated by a cutoff value (visually determined), $DPD = 0.7$ (Figure 4c). For the DPD matrix, values are necessarily 1 along the diagonal, as the subnetworks are compared to themselves. Regions of symmetry along the diagonal that contain high DPD values ($DPD > 0.7$) indicate subnetworks that share more than 70% of influx (Figure 4b).

Using the cutoff value of $DPD = 0.7$, three lobes are interpreted from the DPD matrix (Figure 5). Identified lobes include a western lobe, consisting of outlets $1-18$, and an eastern lobe, consisting outlets $24-32$; there is no predicted flux shared between the two lobes (Figures 5a). Subnetworks (outlets) $19-23$ share flux with the entire delta, and are therefore grouped together and classified as a central lobe. This interpretation of lobes agrees with previous assessments (Figure 5a; Il'icheva, 2008; Il'icheva et al., 2015), as well as with spatial trends in shoreline progradation rates (Figure 5b). Boundaries between the lobes are set at opening angles $\Theta = 65^o$ and $\Theta = 137^o$, which are the mean values of the angles measured based on the three described methods for distinguishing lobes (Figure 5c).

4.2 Remotely-sensed data

4.2.1 Basin and delta characteristics: slope and depth

Bathymetry data analyses indicate that basin slope and depth are highly variable for the three Selenga Delta lobes (Figure 6; Table 1). The central lobe has a basin slope of $2.20 \pm 0.60 \times 10^{-2}$. The western and eastern lobes are surrounded by embayments, and therefore do not have clear division between delta topset and foreset (Figure 6a and c). For these two lobes, basin slope (i.e., foreset slope) is assumed to be the angle of repose

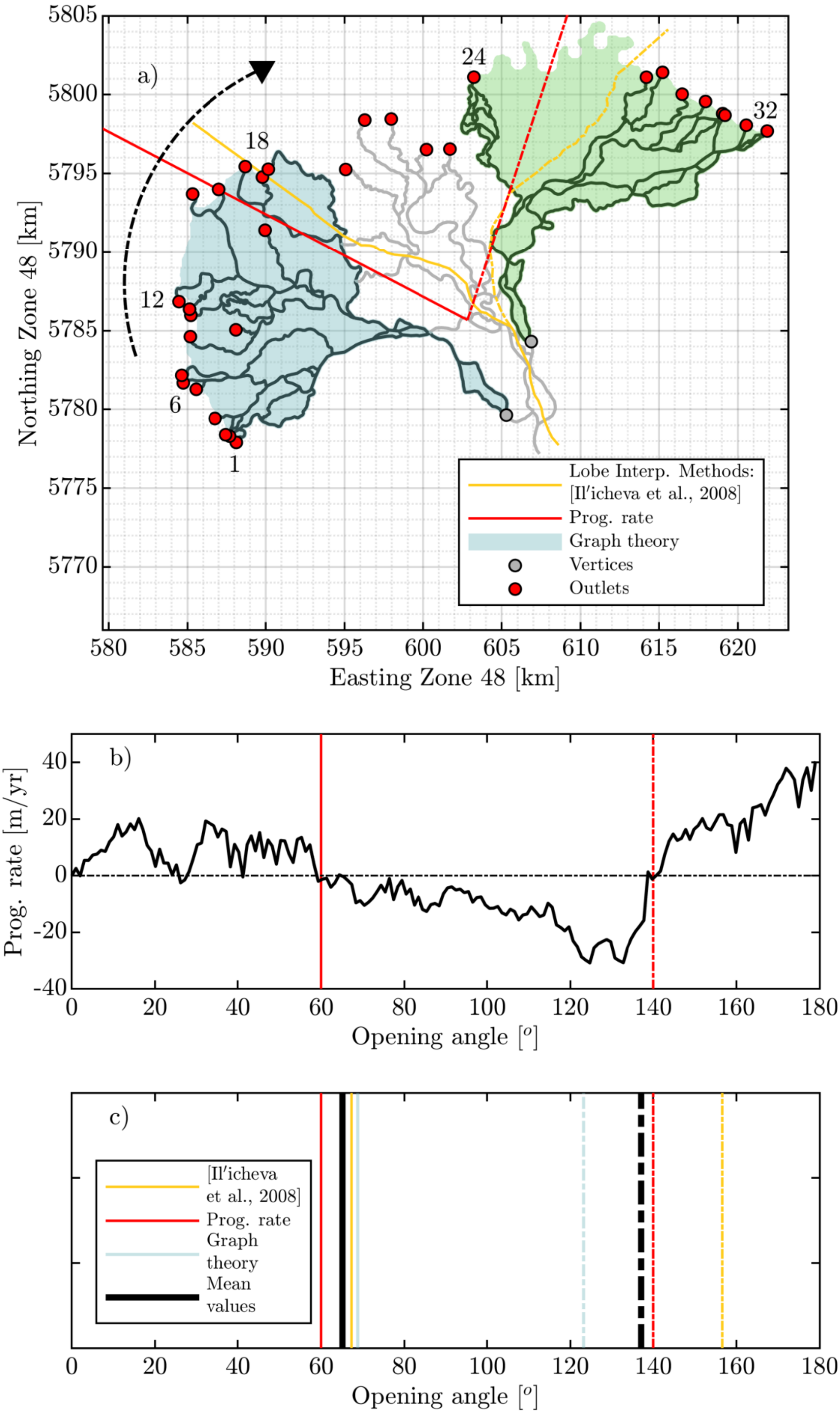

Figure 5. a) Delta lobes are distinguished using three methods: graph theory, qualitative assessment, long-term shoreline progradation rates ($\bar{R}_{pro}$). b) Progradation rates as a function of transect opening angles along the delta. c) Delta lobe boundaries identified using aforementioned methods. The mean opening angles are $\Theta = 65^o$ and $\Theta = 137^o$ (i.e., solid and dashed lines for the western/central and central/eastern lobe boundaries, respectively.

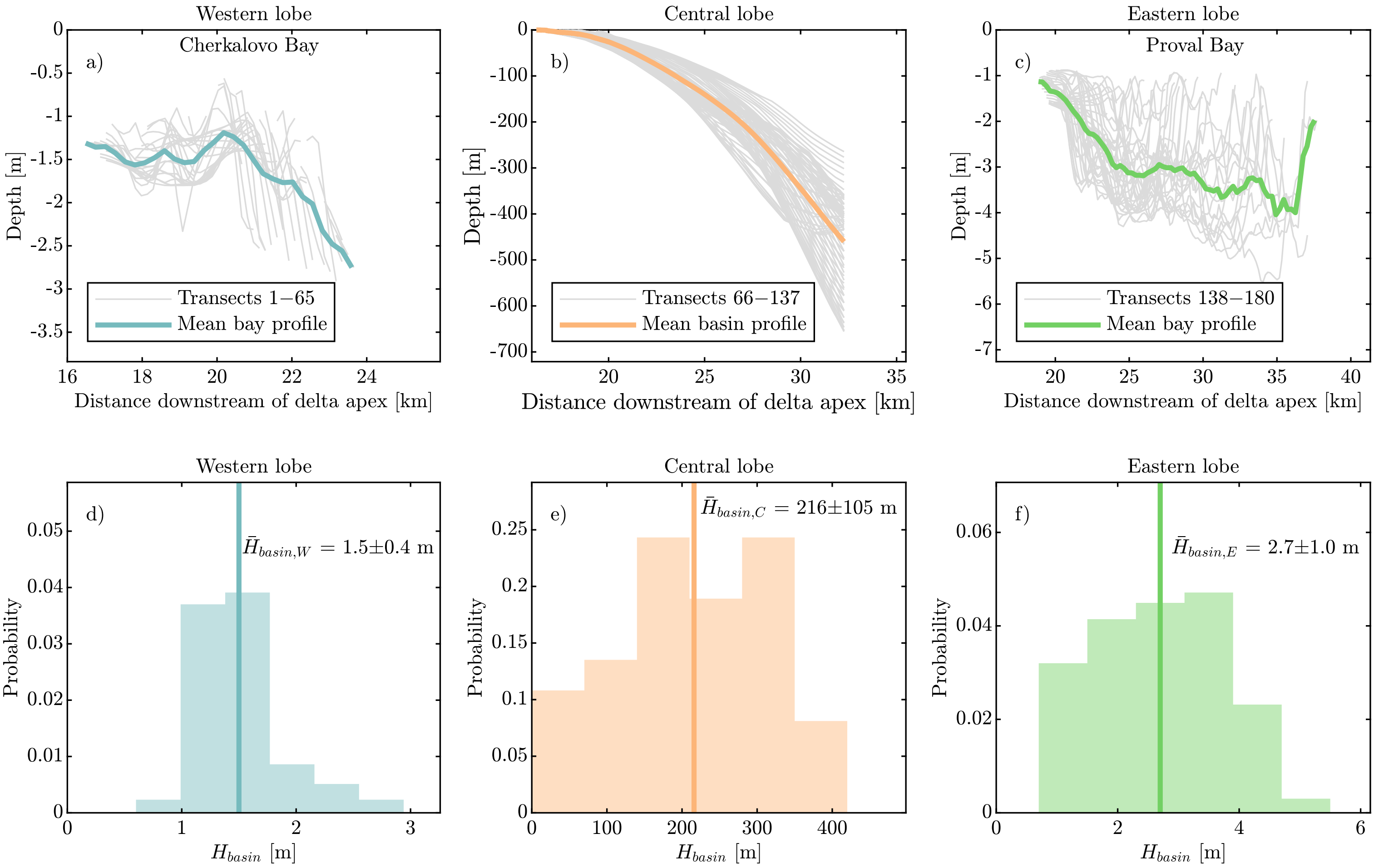

Figure 6. Water depth profiles from the a) western, b) central, and c) eastern lobes of the Selenga River delta, as measured from the sampling transects. d-e) Probability distributions of basin water depth measured for each lobe.

for fine-grained sediment, 30°−32° (Piliouras et al., 2017; Wang et al., 2019). Basin depth of the central lobe is 216±105 m (Figure 6e). For the western and eastern lobes, embayment bathymetry reveals a mean depth of, respectively, Cherkalovo Bay: 1.5±0.4 m; and Proval Bay: 2.7±1.0 m (Figure 6d and f).

Analysis of the NASA SRTM data show that topset slopes are variable for the three lobes (Figure 7a−c; Table 1). The eastern lobe maintains the shallowest topset slope (2.70±0.42 x 10^{-4}). The topset slope of the central lobe is 3.80±0.42 x 10^{-4}, 41% steeper than the eastern lobe. The topset slope of the western lobe is 3.42±0.36 x 10^{-4}. Based on field surveys of the seven main distributary channels from low to bankfull flow in 2016 and 2018, water surface and bed slopes are largest for channels in the western lobe (2.24±0.04

and 1.88±0.41 x 10^{-4}, respectively), followed by the eastern (1.84±0.03 and 1.65±0.51 x 10^{-4}, respectively) and central lobes (1.74±0.11 and 1.05±0.33 x 10^{-4}, respectively; Table 1; Figure 7f). The central lobe has the steepest topset slope, as well as the largest difference between topset and channel bed slope (Table 1; Figures 7f)

Mean topset elevation profiles are compared between the three lobes (Figure 7d). There is little difference in topset elevation ($\Delta\bar{Z}$) near the apex of the three lobes (Figure 7d). Specifically, values of $\Delta\bar{Z}$ for the central/western lobes, and central/eastern lobes are 0.06±0.38 m and 0.29±0.41 m, respectively. However, for regions starting at a distance of 5.0 km downstream of delta apex, the eastern lobe is 1.22±0.53 m higher than the central lobe, thus indicating a lateral gradient, with the central lobe as a relative low. Similarly, for a distance of 10.0 km downstream of the delta apex, the western lobe is 0.42±0.35 m higher than the central lobe. For this study, the area between 5.0 and 10.0 km downstream of apex is termed the region of topset elevation divergence (Figure 7d and e). The mean elevation in this region is 456 m above sea level, and is 1 m higher than mean lake level of 455 m.

4.2.2 Shoreline change

Analysis of the modern deltaic shoreline position indicates that the eastern lobe has the largest modern radius ($\bar{R}$ = 19.9±0.9 km), followed by the western and central lobes ($\bar{R}$ = 17.6±0.6 km and $\bar{R}$ = 16.7±0.6 km, respectively, Figure 8; Table 1). The long-term mean progradation rate, using shoreline position data from 1862 to 2019, is maximum for the eastern lobe, at 19±4 m/yr. Meanwhile, the progradation rate of the western lobe is 12±3 m/yr, and the central lobe is retreating at 14±5 m/yr (Figures 8a−c). Decadal mean progradation rate is decreasing for the eastern lobe since the 1862 event, from 23±16 m/yr to −6±10 m/yr (negative rate indicates shoreline retreat; Figures 8d). Similarly, retreat rate of the central lobe decreased from −18±3 m/yr to −1±7 m/yr (Figures 8f). During the same time interval, progradation rate of the western lobe increased slightly, from 7±2 m/yr to 10±7 m/yr (Figures 8e). Since the 1862 event, the eastern and western lobes have prograded 3.8±2.9 km and 2.7±0.7 km basinward, respectively, while the central lobe has retreated 1.0±1.3 km.

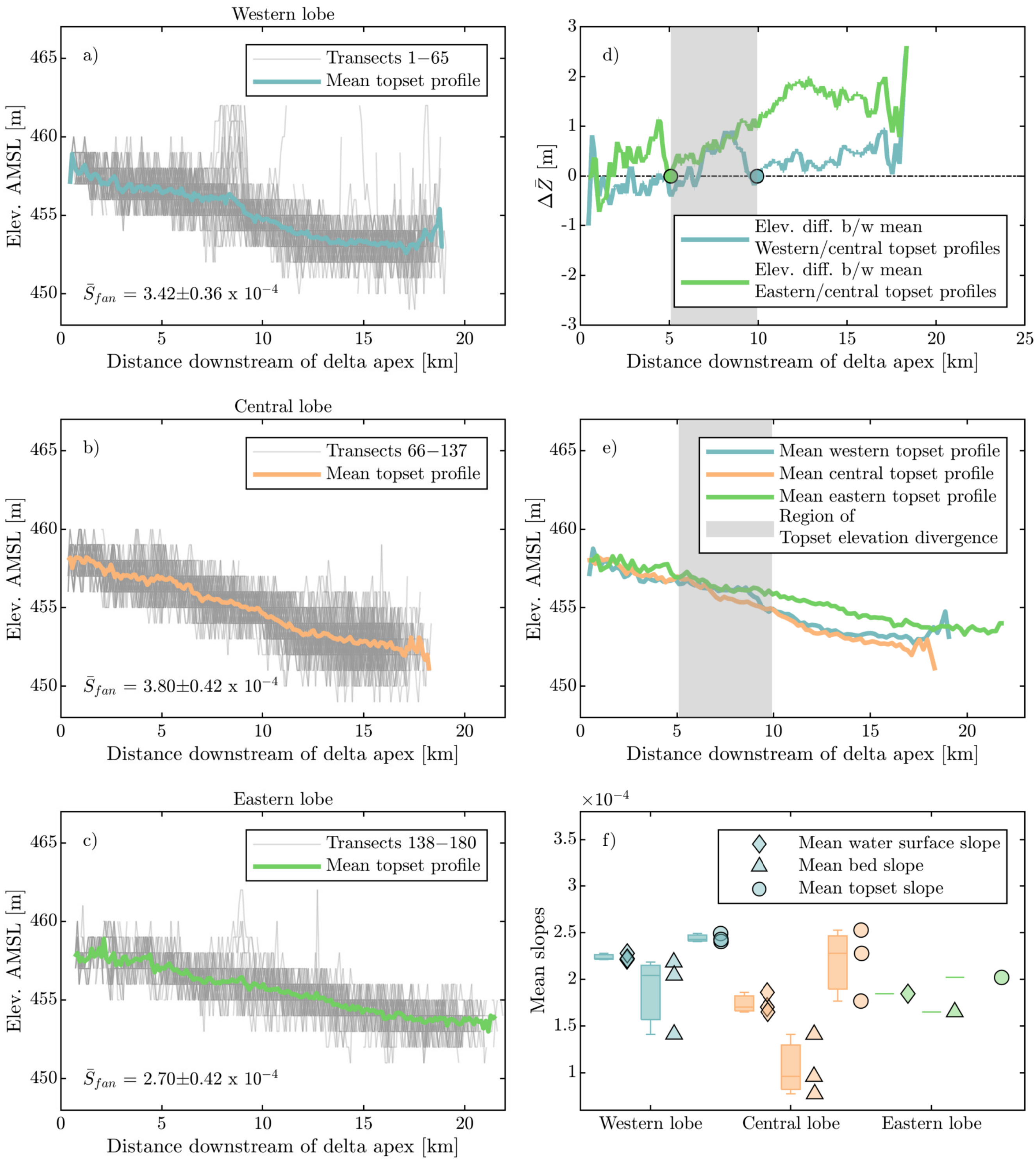

Figure 7. Topset elevations of the a) western, b) central, and c) eastern lobes of the Selenga River delta measured from NASA SRTM data for each of the 180 sampling transects. d) Difference in mean topset elevation ($\Delta\bar{Z}$) between the western/central lobes, and eastern/central lobes, as calculated by subtracting mean profiles. e) Mean topset elevation profiles for the three delta lobes. f) Channel bed and topset slopes for the seven distributary channels in the delta (Figure 1), categorized by lobes.

Table 1. Measured characteristics of the Selenga River delta and its three lobes

	Western lobe	Central lobe	Eastern lobe	Entire delta
Transect No.	1−65	66−137	138−180	1−180
Receiving basin variables:				
Basin slope ($\bar{S}_{basin}$)	0.58−0.63$^{\times}$	2.20±0.60 x 10^{-2}	0.58−0.63$^{\times}$	1.27±0.99 x 10^{-2}
Basin depth ($\bar{H}_{basin}$) [m]	1.5±0.4	216±105	2.7±1.0	133±110
Delta lobe variables:				
Opening angle ($\bar{\lambda}$)	65°	72°	43°	180°
Topset slope ($\bar{S}_{fan}$)	3.42±0.36 x 10^{-4}	3.80±0.42 x 10^{-4}	2.70±0.42 x 10^{-4}	3.41±0.58 x 10^{-4}
*Progradation rate** ($\bar{R}_{pro}$) [m/yr]	12±3	−14±5	19±4	5±4
Lobe radius ($\bar{R}$) [km]	17.6±0.6	16.7±0.6	19.9±0.9	17.9±1.5
Initial lobe radius ($\bar{R}_0$) [km]	15.0±0.4	17.7±1.6	15.6±2.3	16.0±2.2
Change in lobe radius ($\Delta\bar{R}$) [km]	2.7±0.7	−1.0±1.3	3.8±2.9	1.4±2.9
Fraction of flux ($\bar{F}$)	43.6%±10.9%	16.1%±4.9%	40.3%±8.6%	100%
Number of outlets (N)	15	9	8	32
Distributary channel variables:				
Water surface slope ($\bar{S}_{ws}$)	2.24±0.04 x 10^{-4}	1.74±0.11 x 10^{-4}	1.84±0.03 x 10^{-4}*	1.97±0.26 x 10^{-4}
Channel bed slope ($\bar{S}_b$)	1.88±0.41 x 10^{-4}	1.05±0.33 x 10^{-4}	1.65±0.51 x 10^{-4}*	1.49±0.52 x 10^{-4}
Bankfull depth $(\tilde{H}_{bf})^+$ [m]	$2.7\pm^{1.3}_{0.2}$	$2.5\pm^{0.3}_{0.7}$	$2.3\pm^{0.4}_{0.4}$	$2.5\pm^{0.6}_{0.4}$
Bankfull width $(\tilde{B}_{bf})^+$ [m]	$141\pm^{45}_{35}$	$45\pm^{20}_{12}$	$122\pm^{28}_{21}$	$106\pm^{44}_{24}$
Channel length $(\tilde{L}_c)^+$ [m]	$1600\pm^{1190}_{680}$	$1650\pm^{2770}_{990}$	$1480\pm^{2220}_{810}$	$1570\pm^{1620}_{790}$

$^{\times}$ Angle of repose at 30°−32° (Piliouras et al., 2017; Wang et al., 2019)

* Mean±95% confident interval

$^{+}$ Median±75th and 25th percentiles

Other values in this table are mean±one standard deviation (σ)

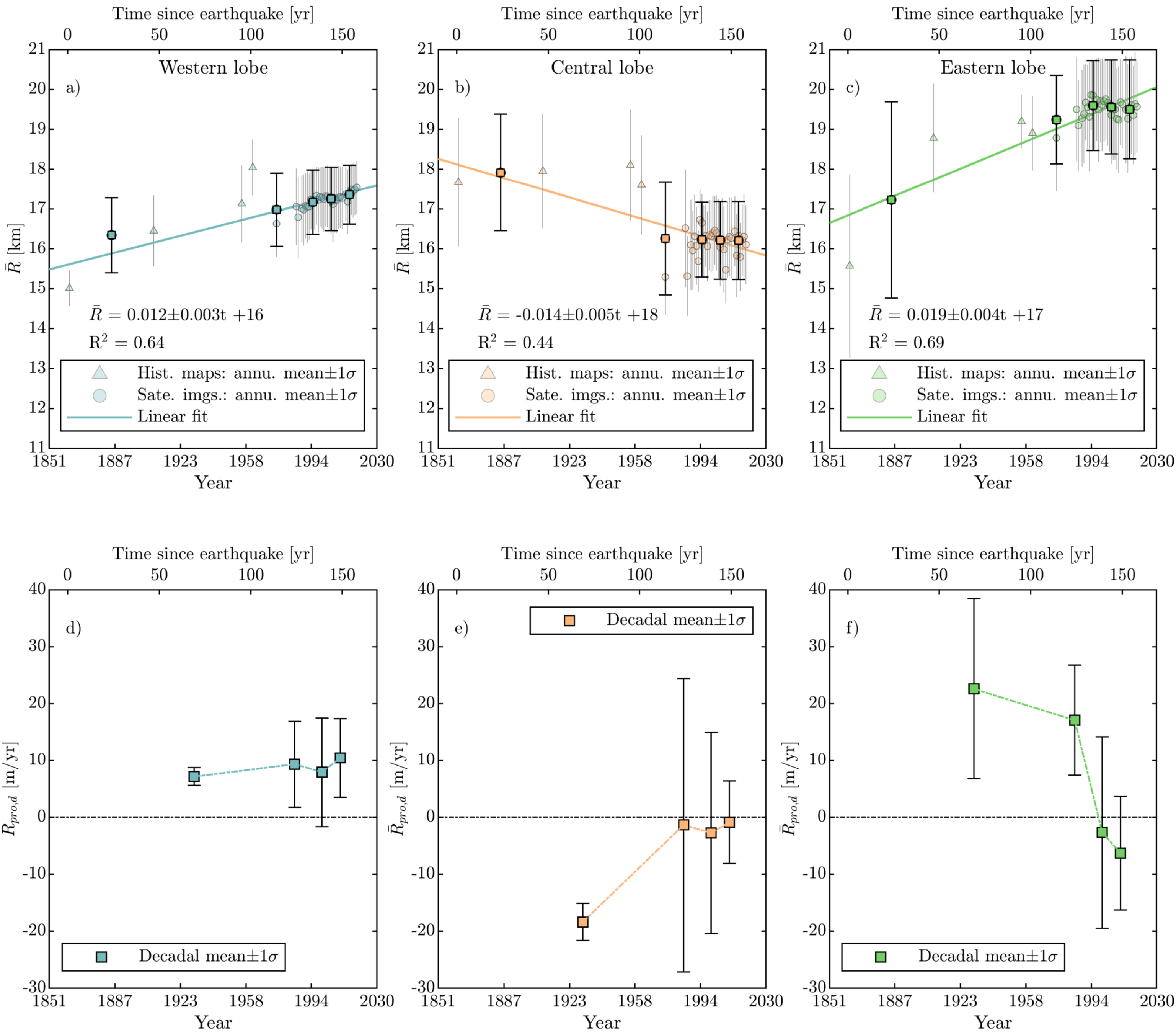

Figure 8. Annual and decadal mean delta radius and progradation rates over time for the western, central, and eastern lobes, since the 1862 earthquake.

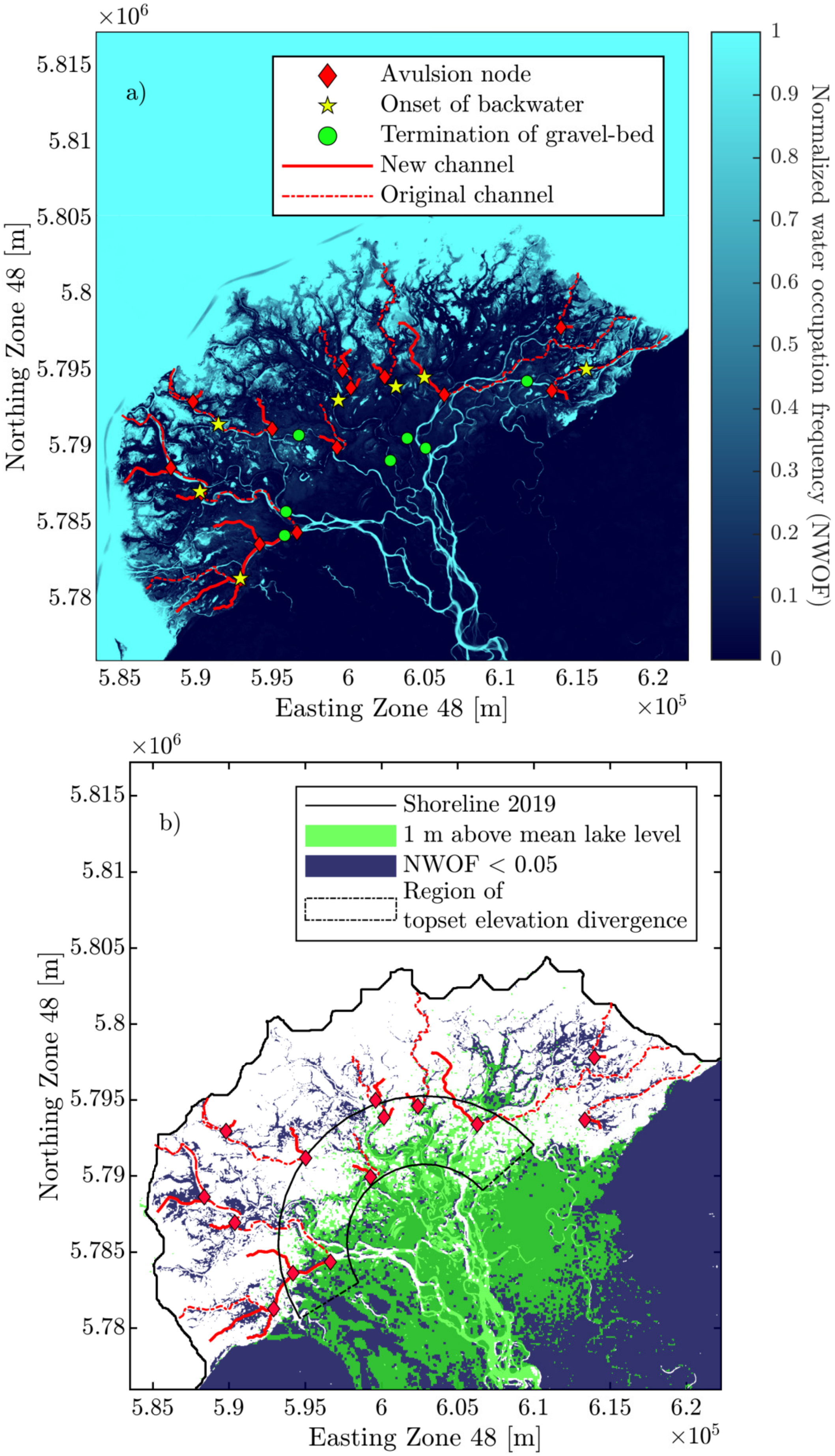

Figure 9. a) Normalized water occupation frequency (NWOF) map, calculated by stacking MNDWI images from 1986−2019. Value of 1 (light blue) indicates areas of continuous water occupation and a value of 0 (dark blue) indicates areas of no water occupation. In addition, locations of backwater influence on flow and downstream limits of gravel for the seven distributary channels are shown (Dong et al., 2016). b) Map showing normalized water occupation frequency values less than 0.05 (indicate dry), overlaid with elevation 1 m greater than mean lake level. The dashed region marks the onset of elevations divergences between eastern/central and western/central lobes, as shown in Figures 7. Avulsion nodes, original, and new channel pathways are overlaid in both panels.

4.2.3 Avulsion sites

A normalized water occupation frequency map (NWOF) shows that the major distributary channels posses high values, indicating water occupation (Figure 9a). Also, this is the case between the distributary channels, where oxbow lakes and abandoned channels are abundant (Figure 9a). Areas of low NWOF values, indicating dry land, are located in the upstream region, near the delta apex, and also adjacent to active channels (e.g., levees; Figure 9a).

A DEM, adjusted to accentuate relatively higher elevation, is compared to a modified map of NWOF showing values < 0.05 (indicating less than 5% water occupation frequency; Figure 9b). The comparison shows that regions near the delta apex are both high and dry, due to relic terraces and active levees of the distributary channels (Figure 9b).

Identified channel avulsions are located in areas downstream of the relatively elevated terraced regions. In total, fourteen avulsion nodes are identified based on NWOF maps and Landsat images. These nodes are distributed amongst the three lobes. Typically, avulsion sites are downstream of the gravel-sand transition, near the region of backwater flow (Dong et al., 2016). Newly avulsed channel pathways usually flow into areas of high NWOF values, indicating avulsions of channels into topographic lows between the major active distributary channels (Figure 9b).

4.3 Field measured distributary channel geometry

Based on field data analysis, channels in the western lobe have the largest median bankfull width and depth ($141\pm^{45}_{35}$ m and $2.7\pm^{1.3}_{0.2}$ m), followed by the eastern and central lobes ($122\pm^{28}_{21}$ m and $2.3\pm^{0.4}_{0.4}$ m; $45\pm^{20}_{12}$ m and $2.5\pm^{0.3}_{0.7}$ m; Table 1; Figures 10b and c). Coefficient of variations (c_v) for width and depth measurements are largest in the central lobe ($c_v = 0.58$ and 0.50), c_v values are 115% and 39% larger than those of the western and eastern lobes, respectively (Figure 10). In contrast, c_v is smaller in the western and eastern lobes, respectively ($c_v = 0.31$ and 0.36; $c_v = 0.27$ and 0.39).

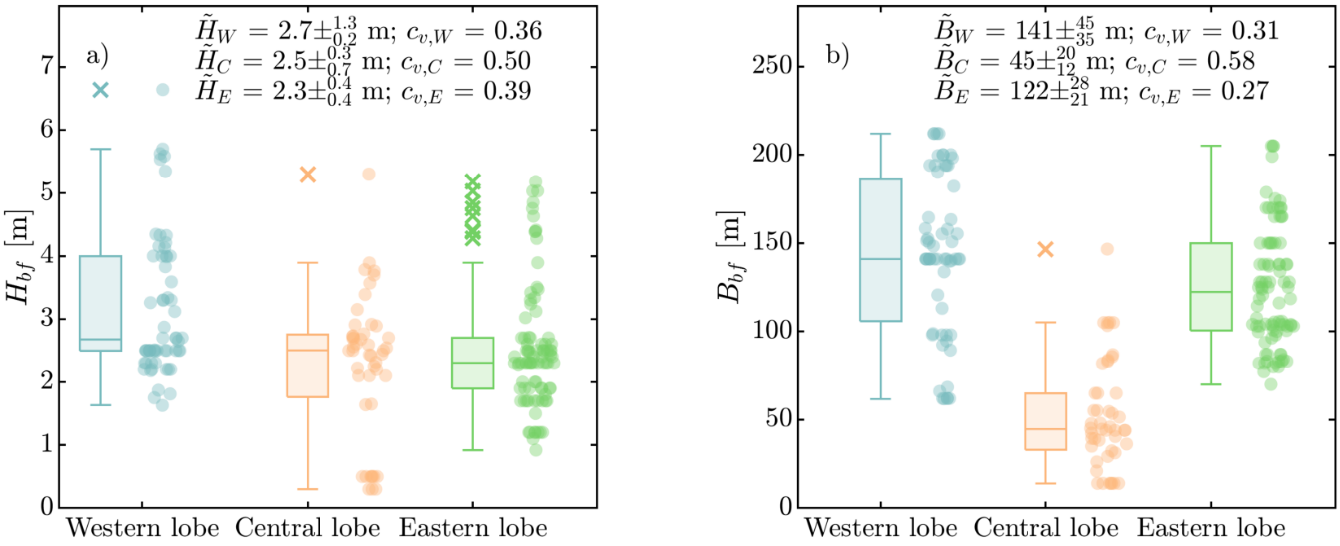

Figure 10. Measured bankfull a) depth (H_{bf}) and b) width (B_{bf}) in channels of the three lobes. Median values±quantiles one and three, and coefficient of variance (c_v) are also indicated.

Table 2. Calculated properties of the Selenga River delta and its three lobes

	Western lobe	Central lobe	Eastern lobe	Entire delta
Transect No.	1−65	66−137	138−180	1−180
Receiving basin variables:				
Tectonic timescale (T_t) [yr]	–	–	–	340−2600
Delta lobe variables:				
Sediment volume ($\Delta\tilde{V}$) [km^3]	$0.17\pm^{0.14}_{0.12}$	$-0.07\pm^{0.17}_{0.18}$	$0.19\pm^{0.12}_{0.11}$	$0.12\pm^{0.14}_{0.15}$
Total sediment discharge (Q_s) [m^3/yr] *	4.82 x $10^5\pm$4.61 x 10^4	1.77 x $10^5\pm$1.70 x 10^4	4.46 x $10^5\pm$4.27 x 10^4	1.10 x $10^6\pm$1.06 x 10^5
Bed material discharge (Q_{bm}) [m^3/yr]*	1.03 x $10^5\pm$9.84 x 10^3	3.78 x $10^4\pm$3.62 x 10^3	9.50 x $10^4\pm$9.10 x 10^3	2.35 x $10^5\pm$2.26 x 10^4
Alluvial grade ($\tilde{G}_{index}$)	$0.67\pm^{0.03}_{0.04}$	$0.009\pm^{0.006}_{0.003}$	$0.50\pm^{0.11}_{0.07}$	$0.49\pm^{0.16}_{0.48}$
Lobe avulsion timescale ($\tilde{T}_{A,l}$) [yr]	$8100\pm^{2800}_{2300}$	1.20 x $10^6\pm^{8.20\text{ x }10^5}_{5.70\text{ x }10^5}$	$9600\pm^{3500}_{2800}$	$12300\pm^{650000}_{4700}$
Distributary channel variables:				
Bed material discharge per channel ($\bar{Q}_{bm,c}$) [m^3/yr]*	6.85 x $10^3\pm$6.56 x 10^2	4.20 x $10^3\pm$4.02 x 10^2	1.19 x $10^4\pm$1.14x 10^3	7.64 x $10^3\pm$3.77 x 10^3
Channel avulsion timescale ($\tilde{T}_{A,c}$) [yr]	$60\pm^{50}_{30}$	$20\pm^{30}_{10}$	$20\pm^{20}_{10}$	$30\pm^{60}_{20}$

* rating curve predicated values with ±95% confident interval

other values in this table are median with ±75$^{\text{th}}$ and 25$^{\text{th}}$ percentiles

4.4 Delta lobe volumes, sediment discharge, and avulsion timescales

The calculated volume of sediment deposition above mean lake level since the 1862 earthquake event is highest in the eastern lobe ($0.19\pm^{0.12}_{0.11}$ km^3), followed by the western lobe ($0.17\pm^{0.14}_{0.12}$ km^3; Equations 6 and 7; Figure 11a). However, since 1862, sediment volume in the central lobe is sequestered below mean lake level by $0.07\pm^{0.17}_{0.18}$ km^3 (Table 2; Figure 11a). Mean annual sediment discharge (Q_s) entering the delta at the apex is calculated at 1.10 x $10^6\pm$1.06 x 10^5 m^3/yr (Equation 8). Of this total discharge, mean annual bed material load (Q_{bm}) is 2.35 x $10^5\pm$2.26 x 10^4 m^3/yr. This value is used to calculate both channel and lobe avulsion timescales ($D \geq 0.0625$ mm; 21.3% of the total load; Table 2).

Grade index (G_{index}) are variable for the three lobes (equations 1): $0.67\pm^{0.03}_{0.04}$ for the western lobe, $0.009\pm^{0.007}_{0.003}$ for the central lobe, and $0.050\pm^{0.11}_{0.07}$ for the eastern lobe (Table2; Figure 11b). The characteristic autogenic lobe avulsion timescales ($T_{A,l}$; equation 9) are $8100\pm^{2800}_{2300}$, 1.20 x $10^6\pm^{8.20\text{ x }10^5}_{5.70\text{ x }10^5}$, and $9600\pm^{3500}_{2800}$ years for the western, central, and eastern lobes, respectively (Figure 11c). The characteristic channel avulsion timescale ($T_{A,c}$; equation 10) is $60\pm^{50}_{30}$ years for the western lobe, $20\pm^{30}_{10}$ years for the central lobe, and $20\pm^{20}_{10}$ years for the eastern lobe, which are all significantly shorter than the lobe avulsion timescales (Table 2; Figure 11d). The the characteristic lobe and channel avulsion timescales for the entire delta are $T_{A,l} = 12300\pm^{650000}_{4700}$ years and $T_{A,c} = 30\pm^{60}_{20}$ years, respectively (Table 2).

5 Discussions

5.1 Impacts of tectonic subsidence on basin depth and delta avulsion processes

Tectonic activity near the Selenga Delta generates discrete subsidence events that create shallow embayments along delta front (Figure 6). As a result, receiving basin depth is variable for each of the three Selenga Delta lobes, affecting avulsion processes operating over temporal scales of multiple centuries to millennia ($> 10^2 - 10^3$ years; Figure 12a). Avulsions at the delta lobe scale arise due to tectonic subsidence, an allogenic process, that operates at a characteristic length of ∼20 km (Table 2; Figure 12a). The 1862 event triggered an avulsion, steering distributary channels into the newly formed Proval Bay, i.e., from central to eastern lobes (Figure 1; Vologina et al., 2010; Shchetnikov et

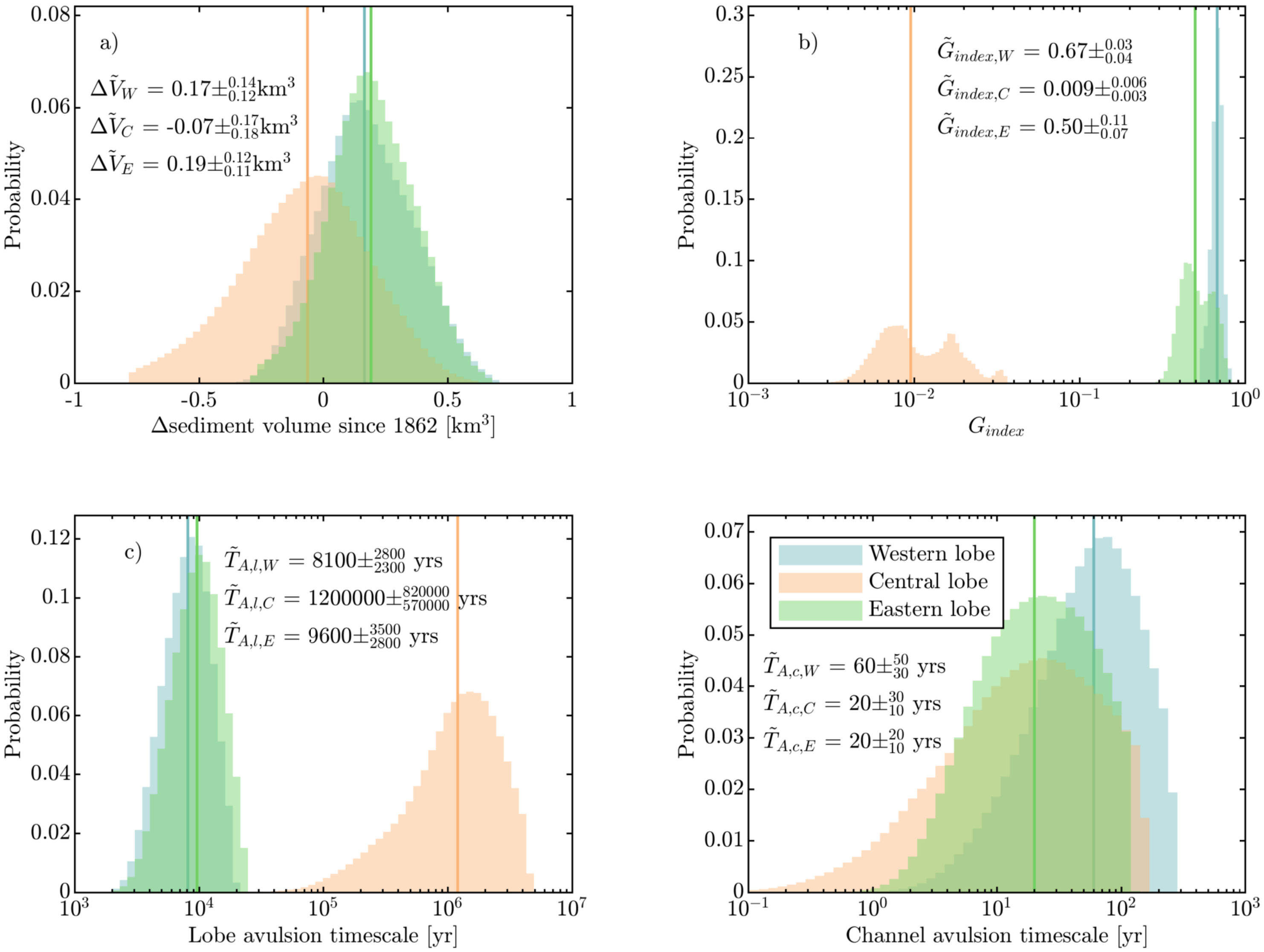

Figure 11. Calculated probability distributions for the three delta lobes: a) change in sediment volume since the 1862 earthquake (ΔV_t), b) grade index (G_{index}), characteristic c) lobe ($T_{A,l}$) and d) channel ($T_{A,c}$) avulsion timescale. Solid lines indicate the median values.

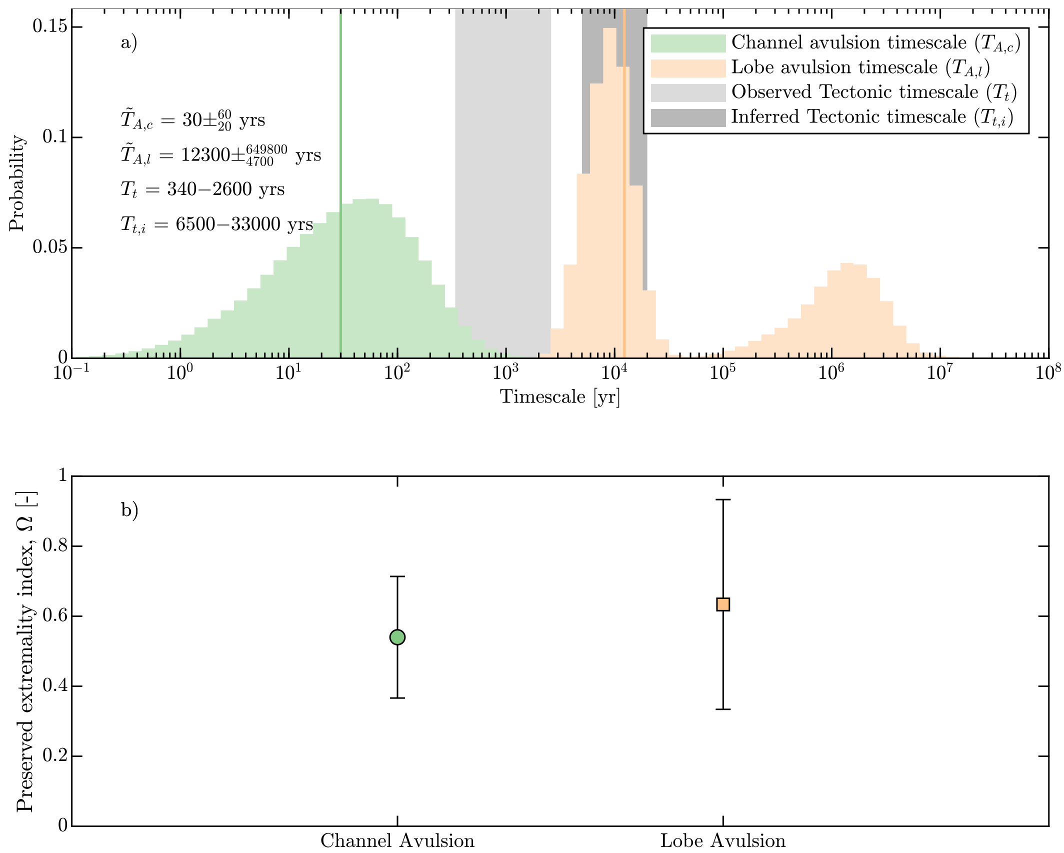

Figure 12. a) Composite probability distributions of channel and lobe avulsion timescales for the three delta lobes ($T_{A,c}$ and $T_{A,l}$, respectively), overlaid with the range of observed and inferred tectonic timescales (T_t and $T_{t,i}$, respectively). Solid lines indicate the median values. b) Preserved extremality index (Ω) for the two avulsion processes that operate on the Selenga Delta: channel and lobe avulsions (Ganti et al., 2020). $\Omega \rightarrow 1$ indicates that the sedimentary system preferentially preserve the largest topographic relief (e.g., delta channel at the main stem), while $\Omega \rightarrow 0$ indicates preferential preservation of the most common topographic relief (e.g., distal distributary channels). Error bars indicate standard deviation.

al., 2012). A subsidence event of similar magnitude is suspected to have formed Cherkalovo Bay, driving reorganization of the distributary channels, and diverting water and sediment from the central to western lobes (Shchetnikov et al., 2012; Moodie & Passalacqua, 2021).

During the intervening period, distributary channel avulsions occur over a characteristic length scale of ∼2 km (i.e., 6 main channel widths), and timescale of decades to centuries (Table 2; Figure 12a). These avulsions are situated in the backwater transitional reach, downstream of the gravel-sand transition and alluvial terraces, and thus likely arise due to autogenic processes, including in-channel sediment aggradation caused by lowering shear stress and sediment transport capacity (Figure 9a; Nittrouer et al., 2012; Dong et al., 2016). Additional factor that may facilitate channel avulsions is the construction of Irkutsk Hydroelectric Power Plant in the 1960s, by which has increased lake level by ∼1 m (Il'icheva et al., 2015).

Distributary channels are avulsing into adjacent low regions between the major active channels. Similar behaviors of compensational filling are also observed in experimental deltas (Figures 9b; Jerolmack & Paola, 2007; Straub et al., 2009). Taking the recent Kazanova channel avulsion (1989) as an example, water and sediment discharge are diverted from the eastern lobe into the central lobe, due to the lateral gradient advantage (Figure 1 and 7d, e; Dong et al., 2020; Aminjafari et al., 2021). As a result, shoreline progradation rates in the eastern lobe have reduced in time, from 23 ± 16 to -6 ± 10 m/yr (negative value indicates shoreline retreat), while of the central lobe have change from -18 ± 3 m to -1 ± 7 m/yr, indicating that sediment is nourishing the central lobe and limiting shoreline retreat (Table 1; Figure 8e, f).

The scale separation in avulsion lengths has been postulated to be associated with formation mechanism of the distributary channels (Jerolmack & Swenson, 2007; Salter et al., 2018; Shaw et al., 2018). Backwater-effect induced distributary channels have length scale of $\sim10-100$ main channel widths, whereas mouth-bar-induced distributary channels have length scale of $\sim1-10$ main channel widths (Jerolmack & Swenson, 2007; D. Edmonds & Slingerland, 2007; Shaw et al., 2018). For the Selenga Delta, the separation in avulsion length scale is caused by the differences between frequency and magnitude of the allogenic and autogenic avulsion processes. However, regardless the types of avulsion processes, a majority of the distributary channel bed profiles are continuously adjusting, thus affecting the condition of alluvial grade for the Selenga Delta.

5.2 Impacts of tectonic subsidence on alluvial grade

Previous experimental studies suggest that a modern river at alluvial grade is most likely to be found in front of a very deep basin (Muto et al., 2016). Due to tectonic subsidence, receiving basin depth is variable around the Selenga Delta, resulting in a range of alluvial grade conditions. The western and eastern lobes are not at alluvial grade, as indicated by the calculated Grade Index, because in-channel sediment aggradation causes distributary channel avulsions (Tabel 2; Figure 11b). These avulsions occur frequently due to low ratio of accommodation (i.e., shallow embayments) to sediment discharge at the delta front, as supported by a low filling index of $B = 0.03$, calculated using mean subsidence rate between earthquakes of $0.02-0.03$ mm/yr (equation 2; Urabe et al., 2004; Liang et al., 2016). Geometry and bed profiles of the newly avulsed channels are continuously adjusting. As a result, the difference in western and eastern lobe slopes is small for both the topset and channel bed (Table 1; Figure 7d-f), while variability in bankfull channel depth and width are also limited (Table 1; Figure 10). Similar patterns of slopes and channel geometry have been observed in experimental deltas that are not at alluvial grade (Muto et al., 2016; Carlson et al., 2018). In contrast to the western and eastern lobes, the central lobe is close to alluvial grade ($G_{index}=0.009\pm^{0.007}_{0.003}$; Table 1; Figure 11b). The central lobe possesses a large difference between topset and channel bed slopes, indicating that the main distributary channels have aggraded the topset profile (Table 1; Figure 7d-f; Carlson et al., 2018). The central lobe is also topographically lower than the other two lobes because it receives less sediment historically (Table 1; Figure 7d, e and 9b). Hydraulic geometry of distributary channels in the central lobe have adjusted to a reduced flow, as it is evident by the fact that they maintain the smallest mean bankfull width and depth of the delta (Table 1; Figure 10).

Findings from this study suggest that a range of channel profiles (i.e., alluvial grade conditions) co-exist on deltas at active margins due to tectonic subsidence, implying a range of sediment transport states to the channel mouths. For example, channels at alluvial grade would be in a state of bypass, whereby sediment is delivered to the foreset, and channels that are not at alluvial grade would rework relic deltaic deposits via avulsion and migration, thus potentially building and preserving diagnostic stratal patterns in the sedimentary record.

5.3 Impacts of tectonic subsidence on the development of deltaic stratigraphy

Discrete tectonic subsidence events are expected to affect the development of stratigraphy at the Selenga Delta. We hypothesize that strata from the Selenga system is built by discrete stratal packages, representing the localized downwarpped volume produced by the seismic events. Furthermore, discrete stratal packages should be separated by laterally continuous fine-grain sediment, deposited within the subsided embayments. Subsequent delta progradations then build coarse-grained topset and foreset deposits (i.e., clinoforms) over this fine-grained layer. Stacking pattern of such discrete stratal package is analogous to parasequences, but has a different formation mechanism (Neal et al., 2016). Specifically, whereas parasqeuences are often interpreted to be driven by eustatic sea level cycles, stratal packages at the Selenga Delta are caused by tectonic subsidence. This hypothesis is supported by seismic data collected by Colman et al. (2003), showing multiple prograding clinoform units that contain well-defined sigmoidal internal reflections, bounded by uniform thickness reflections, i.e., fine-grained draped unit. These units are interpreted as deposits of delta topsets and are measured in current water depth of 100−400 m (C. A. Scholz & Hutchinson, 2000; Colman et al., 2003). Assuming mean subsidence of 3−4 m per event and 25% porosity of unconsolidated mixed sand and gravel for compaction (Leopold et al., 1964), the depth of these delta deposits could imply 20−100 subsidence events (Vologina et al., 2010; Shchetnikov et al., 2012; Lunina & Denisenko, 2020). The age at base of the draped unit that overlay these delta deposits is 650 k.y., thus providing a characteristic recurrence interval of tectonic subsidence at 6500−33000 years (C. A. Scholz & Hutchinson, 2000; Colman et al., 2003). While this inferred tectonic timescale ($T_{t,i}$) is longer than the observed tectonic timescale ($T_t = 340{-}2600$ years), it is comparable to the autogenic lobe avulsion timescale ($T_{A,l} = 12300 \pm^{651200}_{4700}$ years), supporting the notion that tectnoic subsidence controls delta lobe building for the Selenga system (Figure 12a).

Similar style of subsidence and preservation is observed in other active rift basins, such as Lake Malawi and Tanganyika near the East African Rift (C. Scholz et al., 1998). Conventional assumption of time-continuous subsidence in analyzing deltaic stratigraphy would interpret the stacked delta topset deposits observed in these systems as a results of lake level fall (Urabe et al., 2004). However, findings from this study suggest that such stratal patterns could emerge solely due to tectonic subsidence. Herein, we suggest that future studies on deltaic stratigraphy at active margins to use indicators of discrete subsidence events (earthquakes), such as soft-sediment deformation structures (Tanner et al., 2011), to guide stratigraphic interpretations.

The hierarchical avlusion processes at the Selenga Delta is expected to affect size of the sedimentary structures persevered in the discrete stratal packages. We use the preserved extremality index (Ω) to assess the effect of morphodynamic reworking on the characteristic channel dimensions (i.e., sand body sizes) preserved within each package (Ganti et al., 2020), calculated based on the two levels of morphodynamic hierarchy that modify regional relief of the Selenga Delta: distributary channel and delta lobe avulsions, respectively. The calculated preserved extremality indices are $\Omega = 0.54 \pm 0.18$ and 0.64 ± 0.29, for channel and lobe avulsions, respectively, indicating that the hierarchical processes are expected to preferentially preserve deeper channels within each stratal package (Figure 12b). Hence, preserved channel sand bodies may be very similar in size ($3-4$ m deep), contrasting the distribution found for the modern channels, which possess variable width and depth (one order of magnitude differences), ranging from $10-330$ m and $0.3-7.0$ m, respectively (Figure 10; Dong et al., 2016, 2019). The predicted channel patterns occur because the lobe auvlsion timescales are much longer than the channel avulsion timescale ($T_{A,l}/T_{A,c} = 37 \pm^{93}_{24}$), and so distributary channels are able to rework relic deposits during quiescence period between impactful earthquakes (Table 2; Ganti et al., 2020). However, future work to obtain high-resolution subsurface data is necessary to validate our predictions on preservation of sedimentary structures of the Selenga Delta.

6 Conclusions

In this study, field and remotely-sensed delta-lobe and receiving basin characteristics from the Selenga Delta are used to assess the effects of tectonic subsidence on basin depth and delta lobe building. For the Selenga Delta, discrete tectonic subsidence events modify basin depth around the coastline by downdropping a portion of the topset (30% of the modern subaerial delta area) below mean channel depth (3 m). The recurrence interval of these impactful events are shorter than autogenic lobe avulsion timescales ($340-2600$ years versus 12300 years, respectively). Thus, lobe avulsion is triggered predominately by tectonic subsidence, an allogenic process, whereby water and sediment flow are attracted to the newly formed accommodation (partially subsided lobe) due to a regional gradient advantage. During quiescent periods between the subsidence events, channel-scale avulsion occurs more frequently (30 years) due to an autogenic process: in-channel sediment aggradation caused by the backwater effect. As a result, water and sediment are dispersed to topographic lows between the active channels and to the shoreline, so as to generate semicircular delta geometry. Each subsidence event is expected to be preserved as a discrete stratal package that record evidence of morphodyanmic reworking by channel avulsion, leading to preferential preservation of deeper channel. As rift basins are ubiquitous sediment sinks, results from this study indicate basin modeling in tectonic active regions should consider the effects of discrete subsidence events and spatial heterogeneous receiving basin depth, when considering stratigraphic models.

Acknowledgments

This research is supported by funding from AAPG Foundation Grants-in-Aid, GSA Graduate Student Research Grant, University of Wyoming, and National Science Foundation grant EAR-1415944. The research work on which this manuscript is based was carried out in cooperation with the international research initiative Basenet (Baikal-Selenga Network). E. Il'icheva and M. Pavlov are supported by RFBR grant No.17-29-05052, and at the expense of the state task (state registration number AAAA-A21-121012190059-5). We thank students and staff from Irkutsk State, Saint Petersburg State, and Lomonosov Moscow State University for their assistance during the field surveys.

References

Aminjafari, S., Brown, I., Chalov, S., Simard, M., Lane, C. R., Jarsjö, J., … Jaramillo, F. (2021). Drivers and extent of surface water occurrence in the selenga river delta, russia. *Journal of Hydrology: Regional Studies*, *38*, 100945.

Carlson, B., Piliouras, A., Muto, T., & Kim, W. (2018). Control of basin water depth on channel morphology and autogenic timescales in deltaic systems. *Journal of Sedimentary Research*, *88*(9), 1026–1039.

Chadwick, A., Lamb, M., Moodie, A., Parker, G., & Nittrouer, J. (2019). Origin of a preferential avulsion node on lowland river deltas. *Geophysical Research Let-*

ters, *46*(8), 4267–4277.

Chalov, S., Thorslund, J., Kasimov, N., Aybullatov, D., Il'icheva, E., Karthe, D., … others (2016). The selenga river delta: a geochemical barrier protecting lake baikal waters. *Regional Environmental Change*, 1–15.

Chalov, S. R., Jarsjö, J., Kasimov, N. S., Romanchenko, A. O., Pietroń, J., Thorslund, J., & Promakhova, E. V. (2015). Spatio-temporal variation of sediment transport in the selenga river basin, mongolia and russia. *Environmental Earth Sciences*, *73*(2), 663–680.

Colman, S. M. (1998). Water-level changes in lake baikal, siberia: tectonism versus climate. *Geology*, *26*(6), 531–534.

Colman, S. M., Karabanov, E., & Nelson III, C. (2003). Quaternary sedimentation and subsidence history of lake baikal, siberia, based on seismic stratigraphy and coring. *Journal of Sedimentary Research*, *73*(6), 941–956.

DeBatist, M., & Charlet, F. (2007). Bathymetry of lake baikal.

Dong, T. Y., Nittrouer, J. A., Czapiga, M. J., Ma, H., McElroy, B., Il'icheva, E., … Parker, G. (2019). Roles of bank material in setting bankfull hydraulic geometry as informed by the selenga river delta, russia. *Water Resources Research*, *55*(1), 827–846.

Dong, T. Y., Nittrouer, J. A., Il'icheva, E., Pavlov, M., McElroy, B., Czapiga, M. J., … Parker, G. (2016). Controls on gravel termination in seven distributary channels of the selenga river delta, baikal rift basin, russia. *Geological Society of America Bulletin*, *128*(7-8), 1297–1312.

Dong, T. Y., Nittrouer, J. A., McElroy, B., Il'icheva, E., Pavlov, M., Ma, H., … Moreido, V. M. (2020). Predicting water and sediment partitioning in a delta channel network under varying discharge conditions. *Water Resources Research*, e2020WR027199.

Edmonds, D., & Slingerland, R. (2007). Mechanics of river mouth bar formation: Implications for the morphodynamics of delta distributary networks. *Journal of Geophysical Research: Earth Surface*, *112*(F2).

Edmonds, D. A., Paola, C., Hoyal, D. C., & Sheets, B. A. (2011). Quantitative metrics that describe river deltas and their channel networks. *Journal of Geophysical Research: Earth Surface*, *116*(F4).

Galazy, G. (1993). Baikal, atlas (in russian).

Ganti, V., Chadwick, A. J., Hassenruck-Gudipati, H. J., & Lamb, M. P. (2016). Avulsion cycles and their stratigraphic signature on an experimental backwater-controlled delta. *Journal of Geophysical Research: Earth Surface*, *121*(9), 1651–1675.

Ganti, V., Chu, Z., Lamb, M. P., Nittrouer, J. A., & Parker, G. (2014). Testing morphodynamic controls on the location and frequency of river avulsions on fans versus deltas: Huanghe (yellow river), china. *Geophysical Research Letters*, *41*(22), 7882–7890.

Ganti, V., Hajek, E. A., Leary, K., Straub, K. M., & Paola, C. (2020). Morphodynamic hierarchy and the fabric of the sedimentary record. *Geophysical Research Letters*, *47*(14), e2020GL087921.

Gyninova, A., & Korsunov, V. (2006). The soil cover of the selenga delta area in the baikal region. *Eurasian Soil Science*, *39*(3), 243–250.

Hutchinson, D., Golmshtok, A., Zonenshain, L., Moore, T., Scholz, C., & Klitgord, K. D. (1992). Depositional and tectonic framework of the rift basins of lake baikal from multichannel seismic data. *Geology*, *20*(7), 589–592.

Il'icheva, E. (2008). Dynamics of the selenga river network and delta structure. *Geography and Natural Resources*, *29*(4), 343–347.

Il'icheva, E., Gagarinova, O., & Pavlov, M. (2015). Hydrologo-geomorphological analysis of landscape formation within the selenga river delta. *Geography and Natural Resources*, *36*(3), 263–270.

Jerolmack, D. J., & Mohrig, D. (2007). Conditions for branching in depositional rivers. *Geology*, *35*(5), 463–466.

Jerolmack, D. J., & Paola, C. (2007). Complexity in a cellular model of river avulsion. *Geomorphology*, *91*(3-4), 259–270.

Jerolmack, D. J., & Swenson, J. B. (2007). Scaling relationships and evolution of distributary networks on wave-influenced deltas. *Geophysical Research Letters*, *34*(23).

Kim, W., Mohrig, D., Twilley, R., Paola, C., & Parker, G. (2009). Is it feasible to build new land in the mississippi river delta? *EOS, Transactions American Geophysical Union*, *90*(42), 373–374.

Kim, W., Paola, C., Swenson, J. B., & Voller, V. R. (2006). Shoreline response to autogenic processes of sediment storage and release in the fluvial system. *Jour-*

nal of Geophysical Research: Earth Surface, *111*(F4).

Kim, W., Sheets, B. A., & Paola, C. (2010). Steering of experimental channels by lateral basin tilting. *Basin Research*, *22*(3), 286–301.

Kim, Y., Kim, W., Cheong, D., Muto, T., & Pyles, D. (2013). Piping coarse-grained sediment to a deep water fan through a shelf-edge delta bypass channel: tank experiments. *Journal of Geophysical Research: Earth Surface*, *118*(4), 2279–2291.

Kopp, J., & Kim, W. (2015). The effect of lateral tectonic tilting on fluviodeltaic surficial and stratal asymmetries: experiment and theory. *Basin Research*, *27*(4), 517–530.

Krivonogov, S., & Safonova, I. (2017). Basin structures and sediment accumulation in the baikal rift zone: Implications for cenozoic intracontinental processes in the central asian orogenic belt. *Gondwana Research*, *47*, 267–290.

Leopold, L. B., Wolman, M. G., & Miller, J. P. (1964). Fluvial processes in geomorphology.

Liang, M., Kim, W., & Passalacqua, P. (2016). How much subsidence is enough to change the morphology of river deltas? *Geophysical Research Letters*, *43*(19), 10–266.

Logachev, N. (2003). History and geodynamics of bbikal rift. *J. Geol Geophys. Russian Academy of sciences*, *44*, 391–406.

Logatchev, N. (1974). Sayan-baikal-stanavoy upland. *Uplands of the Pribaikalia and Zabaikalia*, 16–162.

Lunina, O. V., & Denisenko, I. A. (2020). Single-event throws along the delta fault (baikal rift) reconstructed from ground penetrating radar, geological and geomorphological data. *Journal of Structural Geology*, *141*, 104209.

Martinsen, O. J., & Bakken, B. (1990). Extensional and compressional zones in slumps and slides in the namurian of county clare, ireland. *Journal of the Geological Society*, *147*(1), 153–164.

Mats, V. D., & Yefimova, I. M. (2015). Paleogeographic scenario of the late cretaceous–cenozoic for the central part of the baikal region. *Geodynamics & Tectonophysics*, *2*(2), 175–193.

Mohrig, D., Heller, P. L., Paola, C., & Lyons, W. J. (2000). Interpreting avulsion process from ancient alluvial sequences: Guadalope-matarranya system (northern spain) and wasatch formation (western colorado). *Geological Society of America Bulletin*, *112*(12), 1787–1803.

Moodie, A. J., Nittrouer, J. A., Ma, H., Carlson, B. N., Chadwick, A. J., Lamb, M. P., & Parker, G. (2019). Modeling deltaic lobe-building cycles and channel avulsions for the yellow river delta, china. *Journal of Geophysical Research: Earth Surface*, *124*(11), 2438–2462.

Moodie, A. J., & Passalacqua, P. (2021). When does faulting-induced subsidence drive distributary network reorganization? *Geophysical Research Letters*, *48*(22), e2021GL095053.

Moran, K. E., Nittrouer, J. A., Perillo, M. M., Lorenzo-Trueba, J., & Anderson, J. B. (2017). Morphodynamic modeling of fluvial channel fill and avulsion time scales during early holocene transgression, as substantiated by the incised valley stratigraphy of the trinity river, texas. *Journal of Geophysical Research: Earth Surface*, *122*(1), 215–234.

Muto, T., Furubayashi, R., Tomer, A., Sato, T., Kim, W., Naruse, H., & Parker, G. (2016). Planform evolution of deltas with graded alluvial topsets: Insights from three-dimensional tank experiments, geometric considerations and field applications. *Sedimentology*, *63*(7), 2158–2189.

Neal, J. E., Abreu, V., Bohacs, K. M., Feldman, H. R., & Pederson, K. H. (2016). Accommodation succession (δ a/δ s) sequence stratigraphy: observational method, utility and insights into sequence boundary formation. *Journal of the Geological Society*, *173*(5), 803–816.

Nittrouer, J. A., Shaw, J., Lamb, M. P., & Mohrig, D. (2012). Spatial and temporal trends for water-flow velocity and bed-material sediment transport in the lower mississippi river. *Bulletin*, *124*(3-4), 400–414.

Nittrouer, J. A., & Viparelli, E. (2014). Sand as a stable and sustainable resource for nourishing the mississippi river delta. *Nature Geoscience*, *7*(5), 350–354.

Pavlov, M., Il'icheva, E., Vershinin, K., & Kobylkin, D. (2019). Development of the lakes of the selenga river delta in the late holocene, in russian. *Bulletin of the Buryatia State University*, *3*. doi: 10.18101/2587-7148-2019-3-31-43

Pietroń, J., Nittrouer, J. A., Chalov, S. R., Dong, T. Y., Kasimov, N., Shinkareva, G., & Jarsjö, J. (2018). Sedimentation patterns in the selenga river delta under changing hydroclimatic conditions. *Hydrological processes*, *32*(2), 278–292.

Piliouras, A., Kim, W., & Carlson, B. (2017). Balancing aggradation and progradation on a vegetated delta: the importance of fluctuating discharge in depositional systems. *Journal of Geophysical Research: Earth Surface*, *122*(10), 1882–1900.

Posamentier, H. W., & Allen, G. P. (1999). *Siliciclastic sequence stratigraphy: concepts and applications* (Vol. 7). SEPM (Society for Sedimentary Geology) Tulsa, Oklahoma.

Ravnås, R., & Steel, R. J. (1998). Architecture of marine rift-basin successions. *AAPG bulletin*, *82*(1), 110–146.

Reitz, M. D., & Jerolmack, D. J. (2012). Experimental alluvial fan evolution: Channel dynamics, slope controls, and shoreline growth. *Journal of Geophysical Research: Earth Surface*, *117*(F2).

Reitz, M. D., Jerolmack, D. J., & Swenson, J. B. (2010). Flooding and flow path selection on alluvial fans and deltas. *Geophysical Research Letters*, *37*(6).

Reitz, M. D., Pickering, J. L., Goodbred, S. L., Paola, C., Steckler, M. S., Seeber, L., & Akhter, S. H. (2015). Effects of tectonic deformation and sea level on river path selection: Theory and application to the ganges-brahmaputra-meghna river delta. *Journal of Geophysical Research: Earth Surface*, *120*(4), 671–689.

Richards, M., Bowman, M., & Reading, H. (1998). Submarine-fan systems i: characterization and stratigraphic prediction. *Marine and Petroleum Geology*, *15*(7), 689–717.

Salter, G., Paola, C., & Voller, V. R. (2018). Control of delta avulsion by downstream sediment sinks. *Journal of Geophysical Research: Earth Surface*, *123*(1), 142–166.

Scholz, C., Moore, T., Hutchinson, D., Golmshtok, A. J., Klitgord, K. D., & Kurotchkin, A. (1998). Comparative sequence stratigraphy of low-latitude versus high-latitude lacustrine rift basins: seismic data examples from the east african and baikal rifts. *Palaeogeography, Palaeoclimatology, Palaeoecology*, *140*(1), 401–420.

Scholz, C. A., & Hutchinson, D. (2000). Stratigraphic and structural evolution of the selenga delta accommodation zone, lake baikal rift, siberia. *International Journal of Earth Sciences*, *89*(2), 212–228.

Shaw, J. B., Miller, K., & McElroy, B. (2018). Island formation resulting from radially symmetric flow expansion. *Journal of Geophysical Research: Earth Surface*, *123*(2), 363–383.

Shchetnikov, A., Radziminovich, Y. B., Vologina, E., & Ufimtsev, G. (2012). The formation of proval bay as an episode in the development of the baikal rift basin: A case study. *Geomorphology*, *177*, 1–16.

Straub, K. M., Paola, C., Kim, W., & Sheets, B. (2013). Experimental investigation of sediment-dominated vs. tectonics-dominated sediment transport systems in subsiding basins. *Journal of Sedimentary Research*, *83*(12), 1162–1180.

Straub, K. M., Paola, C., Mohrig, D., Wolinsky, M. A., & George, T. (2009). Compensational stacking of channelized sedimentary deposits. *Journal of Sedimentary Research*, *79*(9), 673–688.

Swenson, J. B. (2005). Relative importance of fluvial input and wave energy in controlling the timescale for distributary-channel avulsion. *Geophysical Research Letters*, *32*(23).

Syvitski, J. P., Kettner, A. J., Overeem, I., Hutton, E. W., Hannon, M. T., Brakenridge, G. R., … others (2009). Sinking deltas due to human activities. *Nature Geoscience*, *2*(10), 681.

Tanner, D. C., Bense, F. A., & Ertl, G. (2011). Kinematic retro-modelling of a cross-section through a thrust-and-fold belt: the western irish namurian basin. *Geological Society, London, Special Publications*, *349*(1), 61–76.

Tejedor, A., Longjas, A., Zaliapin, I., & Foufoula-Georgiou, E. (2015a). Delta channel networks: 1. a graph-theoretic approach for studying connectivity and steady state transport on deltaic surfaces. *Water Resources Research*, *51*(6), 3998–4018.

Tejedor, A., Longjas, A., Zaliapin, I., & Foufoula-Georgiou, E. (2015b). Delta channel networks: 2. metrics of topologic and dynamic complexity for delta comparison, physical inference, and vulnerability assessment. *Water Resources Research*, *51*(6), 4019–4045.

Urabe, A., Tateishi, M., Inouchi, Y., Matsuoka, H., Inoue, T., Dmytriev, A., & Khlystov, O. M. (2004). Lake-level changes during the past 100,000 years at lake baikal, southern siberia. *Quaternary Research*, *62*(2), 214–222.

Vologina, E., Kalugin, I., Osukhovskaya, Y. N., Sturm, M., Ignatova, N., Radziminovich, Y. B., ... Kuz'min, M. (2007). Sedimentation in proval bay (lake baikal) after catastrophic flooding of the coastal plain in 1862. In *Doklady earth sciences* (Vol. 417, p. 1315).

Vologina, E., Kalugin, I., Osukhovskaya, Y. N., Sturm, M., Ignatova, N., Radziminovich, Y. B., ... Kuz'min, M. (2010). Sedimentation in proval bay (lake baikal) after earthquake-induced subsidence of part of the selenga river delta. *Russian Geology and Geophysics*, *51*(12), 1275–1284.

Wang, J., Muto, T., Urata, K., Sato, T., & Naruse, H. (2019). Morphodynamics of river deltas in response to different basin water depths: An experimental examination of the grade index model. *Geophysical Research Letters*, *46*(10), 5265–5273.

Wu, S., Xu, Y. J., Wang, B., & Cheng, H. (2021). Riverbed dune morphology of the lowermost mississippi river–implications of leeside slope, flow resistance and bedload transport in a large alluvial river. *Geomorphology*, *385*, 107733.

Xu, H. (2006). Modification of normalised difference water index (ndwi) to enhance open water features in remotely sensed imagery. *International journal of remote sensing*, *27*(14), 3025–3033.